

INFORMATION TO USERS

This manuscript has been reproduced from the microfilm master. UMI films the text directly from the original or copy submitted. Thus, some thesis and dissertation copies are in typewriter face, while others may be from any type of computer printer.

The quality of this reproduction is dependent upon the quality of the copy submitted. Broken or indistinct print, colored or poor quality illustrations and photographs, print bleedthrough, substandard margins, and improper alignment can adversely affect reproduction.

In the unlikely event that the author did not send UMI a complete manuscript and there are missing pages, these will be noted. Also, if unauthorized copyright material had to be removed, a note will indicate the deletion.

Oversize materials (e.g., maps, drawings, charts) are reproduced by sectioning the original, beginning at the upper left-hand corner and continuing from left to right in equal sections with small overlaps.

Photographs included in the original manuscript have been reproduced xerographically in this copy. Higher quality 6" x 9" black and white photographic prints are available for any photographs or illustrations appearing in this copy for an additional charge. Contact UMI directly to order.

**ProQuest Information and Learning
300 North Zeeb Road, Ann Arbor, MI 48106-1346 USA
800-521-0600**

UMI[®]

**DYNAMICS OF TRAVELLING HELICITY FRONTS IN
BACTERIAL FLAGELLA**

by
Daniel Coombs

A Dissertation Submitted to the Faculty of the
**GRADUATE INTERDISCIPLINARY PROGRAM
IN APPLIED MATHEMATICS**
In Partial Fulfillment of the Requirements
For the Degree of
DOCTOR OF PHILOSOPHY
In the Graduate College
THE UNIVERSITY OF ARIZONA

2001

UMI Number: 3023486

UMI[®]

UMI Microform 3023486

Copyright 2001 by Bell & Howell Information and Learning Company.

All rights reserved. This microform edition is protected against
unauthorized copying under Title 17, United States Code.

Bell & Howell Information and Learning Company
300 North Zeeb Road
P.O. Box 1346
Ann Arbor, MI 48106-1346

THE UNIVERSITY OF ARIZONA ©
GRADUATE COLLEGE

As members of the Final Examination Committee, we certify that we have read the dissertation prepared by Daniel Coombs entitled Dynamics of travelling helicity fronts in bacterial flagella

and recommend that it be accepted as fulfilling the dissertation requirement for the Degree of Doctor of Philosophy

Raymond E. Goldstein
Ray Goldstein

7/27/01
Date

Alain Goriely

7/27/01
Date

Timothy Secomb
Timothy Secomb

7/27/01
Date

Date

Date

Final approval and acceptance of this dissertation is contingent upon the candidate's submission of the final copy of the dissertation to the Graduate College.

I hereby certify that I have read this dissertation prepared under my direction and recommend that it be accepted as fulfilling the dissertation requirement.

Raymond E. Goldstein
Dissertation Director Ray Goldstein

7/27/01
Date

STATEMENT BY AUTHOR

This dissertation has been submitted in partial fulfillment of requirements for an advanced degree at The University of Arizona and is deposited in the University Library to be made available to borrowers under rules of the Library.

Brief quotations from this dissertation are allowable without special permission, provided that accurate acknowledgment of source is made. Requests for permission for extended quotation from or reproduction of this manuscript in whole or in part may be granted by the head of the major department or the Dean of the Graduate College when in his or her judgment the proposed use of the material is in the interests of scholarship. In all other instances, however, permission must be obtained from the author.

SIGNED: D. Coombs

ACKNOWLEDGEMENTS

The process of writing this dissertation has been made much easier and more enjoyable by far more people than it is possible to mention. I would particularly like to thank two people: Ray Goldstein and John Kessler. Ray, my dissertation director, suggested the problem this work addresses, and has been very helpful and supportive while still making me be self-sufficient as a researcher. John's enthusiasm for biophysics is infectious. He has asked me more difficult, fascinating questions than anyone else. Ray and John are what I hope to become: scientists that only study the interesting problems.

I am grateful to many of the faculty of the university. Those who have directly helped with this dissertation are Moysey Brio and Juan Restrepo (for assistance with the numerical analysis) and particularly Alain Goriely and Greg Huber (for assistance with the perturbation work and modeling). I also thank Tim Secomb, Greg Eyink and Nick Ercolani for serving on my committee. Thanks are due to Tom Powers for acting as my outside reviewer. Additionally, this dissertation would not exist without the expert computer support of Bob Condon and his staff in the Mathematics Department, and that of Mike Eklund and Phil Goisman in Physics.

I thank the Flinn / IGERT biomathematics initiative for financial support over the last four years. As a Flinn student I had the opportunity to meet many good scientists and mathematicians, both from this university and from elsewhere. I hope that the program continues its success for many years.

My life in the program has been enriched by my classmates. Taking core classes and qualifying exams is not easy, and it would have been much harder over the years without the friendship and help of the members of my classes. Relaxing after work is always easier than exams, but I was very much assisted by many of the other fabulous people I have met here. You know who you are.

This work is dedicated to my parents, who have always been pleased with what I have done but wouldn't mind if I hadn't, and to Maria, who is always an inspiration.

TABLE OF CONTENTS

LIST OF TABLES	6
LIST OF FIGURES	7
ABSTRACT	8
1. INTRODUCTION	9
1.1. Bacterial swimming	9
1.2. Flagellar structure and polymorphism	13
1.3. The Hotani experiment	15
1.4. Discussion	20
2. MODEL	22
2.1. Elasticity of thin rods	22
2.2. Derivation of the PDE model	34
2.3. Rescaling and dimensional analysis	40
2.4. Physical parameters	45
3. PERTURBATION ANALYSES	48
3.1. Bistable twisted rod	48
3.2. Singly stable driven helical rod	56
4. NUMERICAL SIMULATIONS	61
4.1. Numerical methods	61
4.2. Numerical results	76
5. CONCLUDING REMARKS	86
A. LOW REYNOLDS NUMBER HYDRODYNAMICS	88
A.1. Fundamental singularities	88
A.2. Flow field due to a rotating cylinder	90
A.3. Application to modelling bacterial flagella	92
REFERENCES	95

LIST OF TABLES

TABLE 2.1.	Description of filament configurations in intrinsic frame	26
TABLE 2.2.	Model Parameters	40
TABLE 2.3.	Parameter values	45

LIST OF FIGURES

FIGURE 1.1. Schematic diagram of run-and-tumble motility	11
FIGURE 1.2. Schematic diagram of Hotani's results	16
FIGURE 1.3. 3-dimensional diagram of Hotani's results.	17
FIGURE 1.4. Illustration of torque experienced at different points along concatenated helices.	19
FIGURE 2.1. Frenet-Serret frame	23
FIGURE 2.2. Natural frame	25
FIGURE 2.3. Bistable potential	35
FIGURE 2.4. Force balance	39
FIGURE 3.1. Comparison of front propagation speeds for twisted rods with different boundary conditions.	56
FIGURE 3.2. Singly stable helix twist rate under extensive flow.	60
FIGURE 4.1. Tangent and hyperbolic tangent functions	67
FIGURE 4.2. Computational stencil for fourth-order Crank-Nicolson	72
FIGURE 4.3. Ω plot for flow speed less than critical ($U=8\mu\text{m/s}$).	78
FIGURE 4.4. Time series of Ω plots for flow speed close to critical ($U=10\mu\text{m/s}$).	79
FIGURE 4.5. Detailed initial time series of Ω plots for flow speed close to critical ($U=10\mu\text{m/s}$).	80
FIGURE 4.6. Filament configuration time series for flow speed close to critical ($U=10\mu\text{m/s}$).	81
FIGURE 4.7. Time series of Ω plots for flow speed somewhat above critical ($U=13\mu\text{m/s}$).	82
FIGURE 4.8. Short-time filament configuration times series for flow speed somewhat above critical ($U=13\mu\text{m/s}$).	83
FIGURE 4.9. Snapshot of filament configuration for flow speed somewhat above critical ($U=13\mu\text{m/s}$).	84
FIGURE 4.10. Chirality transition frequency as a function of imposed fluid stress.	85
FIGURE 4.11. Initial front velocity against applied fluid flow velocity.	85

ABSTRACT

Twenty years ago the experiments of Hotani revealed that flagellar polymorphism (the ability of bacterial flagellar filaments to take on different quaternary structures, specifically helices of different handedness and pitch) can be generated by fluid stresses of the same magnitude as those that occur during natural swimming. Experimental work including the recent crystallization of flagellin, as well as theoretical studies, show how the packing properties and underlying bistability of flagellin may give rise to different static structures. Hotani's experiments showed dynamic nucleation and propagation of domains of opposing handedness on a single flagellum. Here we present the first theory to explain this phenomenon, which is of great relevance to the study of the bundling-unbundling transition in run-and-tumble behaviour of free-swimming bacteria. Our model, based entirely on measurable, physical properties of flagella, bridges the gap between protein-scale statics and cell-scale dynamics. We generate simulations of flagellar motion under fluid stress that exhibit nucleation rates and transition speeds in quantitative agreement with experiment.

1. INTRODUCTION

Bacteria are ubiquitous. There are estimated to be about 5×10^{30} prokaryotic cells (bacteria, eubacteria and blue-green algae) on earth [1]. It is also estimated that the human body contains 10 times as many bacteria as its own cells. From an ecological standpoint we are bacterial colonies. The careful study of these organisms that surround us and with which we are so intimately related is one of the major themes of biological science.

This dissertation focuses on one small part of the (already small) bacterial world - the elasticity of bacterial flagella. Flagella are long, whip-like helical filaments attached to the cell membrane that some species of bacteria are able to rotate (like the propellor of a ship) in order to swim. As will be described thoroughly in this chapter, these filaments do not act like everyday corkscrews or macroscopic elastic rods. The model that will be described is inspired by and tested using the experimental framework of Hotani [2].

The introductory chapter begins with an overview of bacterial swimming, and then focuses on the bundling - unbundling transition in multi-flagellated bacteria and the underlying properties of the flagella themselves. We then discuss the experimental findings of Hotani and explain the results in qualitative terms. Finally the issue we wish to resolve is stated and placed in a larger scientific context.

1.1. Bacterial swimming

Some bacteria are able to swim. They are able to sense certain stimuli such as temperature, gravity, chemicals or light and swim from unfavourable to favourable regions [3]. There are different ways in which different species can do this, and each relies heavily on the use of the flagellum: a long, slender filament which is mounted

in the cell membrane. Typically, the filament forms a helix which is rotated by a molecular motor in its base, making a corkscrew drive or miniature boat propeller and propelling the cell. The bacteria we shall be concerned with here have multiple (say 5-15) flagella. Some such species (called peritrichously flagellated bacteria) are *Bacillus subtilis*, *Salmonella* and *Escherichia coli*. These are also the species for which most work has been performed to examine the structure and function of the flagella.

As we shall see, the dimensions and structure of such a flagellum vary, but to a first approximation they range in length from about 10 to 20 μm with a diameter of 23nm. For comparison, note that the typical cell body has a diameter of a micron or two. The helical pitch is on the order of a micron and the diameter of the helix is about 0.5 μm . The flagellar motor is itself a fascinating piece of machinery, a tiny (nm-scale) true rotary motor. It is the subject of serious current research [4]. Briefly, it is driven by the proton-motive force across the cell membrane. Most of this force is used to synthesise ATP from ADP as an energy store for the other activities of the cell. The remaining part is used by the flagellar motor [5]. The rotation rate is very high, a few hundred hertz, although amazingly, bacteria exist for which the rotation rate is more than a thousand hertz [6]. The torque of the motor is about 10^{-11} dyne cm, producing 10^{-16}W of power at 20 hertz.

The usual description of multiply-flagellated bacterial swimming is that it 'runs' and 'tumbles' (sometimes 'twiddles'). A run is a straight line swim at perhaps 20 - 30 $\mu\text{m/s}$. Every few seconds the run ends and the cell 'tumbles' in place for a few tenths of a second. The next run then begins in a new direction. It appears that the tumble randomises the direction of the next run event, so it is often said that bacteria execute a (biased) random walk. The mechanism for a bias lies within the motor. Receptors bind repellent (attractant) molecules at the cell surface. This causes a series of changes within the cell leading to a chemical change at the motor switch that causes a bias towards more (less) tumbling events, thus biasing the random walk towards regions with a higher concentration of attractants [7], [8]. Presumably other

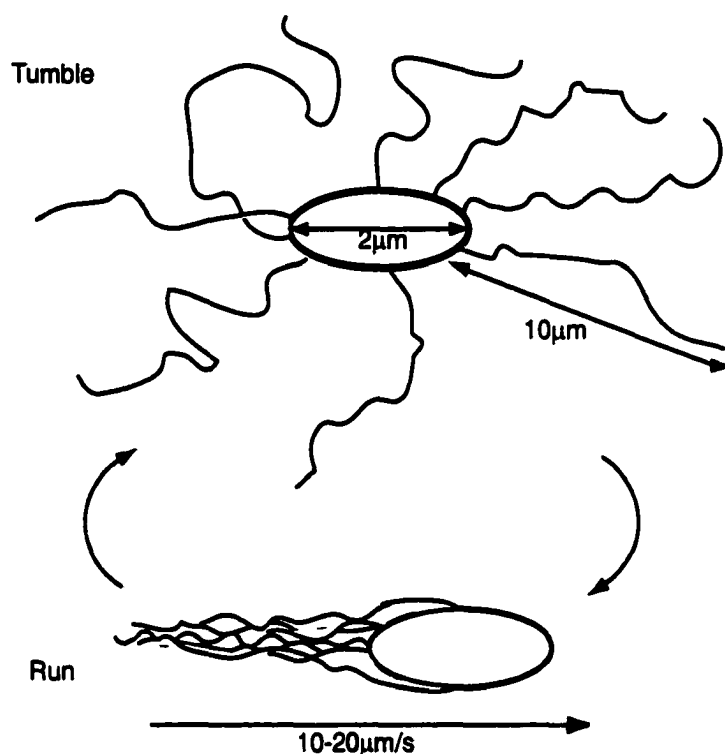


FIGURE 1.1. Schematic diagram of run-and-tumble motility, as first observed by Macnab [10]

stimuli affect the cell in a similar way.

Observations of flagellar bundles seem to have been first made in the 1830s [9]. However the study of single flagella did not really begin until the 1970s. MacNab [10] produced dark-field images of swimming bacteria and Berg [11] tethered a single cell by one flagellum and observed it rotate. The details of these experiments produced the following picture of run and tumble, in which the flagella *bundle* is key.

During a run event, left-handed helical flagella bundle behind the bacterium and turn anticlockwise (when looked at from behind the cell). When the cell decides to tumble, the filaments are turned clockwise and the bundle disperses. During the dispersal, the filaments change handedness from left- to right- handed. It is observed that the change propagates from the cell outwards along each filament [12]. This

is an example of *flagellar polymorphism*, the ability of a single flagellum to exist in geometrically different states. This property is crucial to swimming and is discussed further in section 1.2.

We now ask three fundamental questions regarding flagellar bundling:

1. *What forces act to hold the bundle together during swimming?* Specifically, it is not clear that co-rotating helices will form a stable bundle, or if that bundle will still be able to rotate and produce useful thrust. MacNab partially addressed this question in 1977 [13], by building models to show that there is no geometric hindrance to rotation. This study is significantly augmented by recent work of Powers [14] in which two parallel helices of the same handedness are rotated in a very viscous solution (to reproduce the low-Reynolds-number dynamics of real flagella) and observed to attract each other, interlink and continue to rotate. There is also the very real issue, not addressed by macroscopic experiments, that the local electrical forces between flagella in the bundle are probably of the same order of magnitude as the hydrodynamic forces [15]. The order of magnitude of hydrodynamic forces between flagella in the bundle is discussed in Appendix A.
2. *What forces act to bring the bundle together?* During a tumble, the flagella are not aligned together, and so as they begin to spin (but after they have adopted their left-handed configuration) we might think of them as individual propellers pushing the cell body from a variety of directions. Given that the cell body is asymmetric, thrust along its long axis will be more successful in moving it, causing a drag on filaments aligned along the shorter axis. This drag will tend to align the filaments with the long axis, which is what is observed.
3. *What forces act to break the bundle apart?* We know that a unbundling event is initiated when the cell reverses the directions of the flagellar motors. This is believed to cause a wave of helix-hand reversal to pass outward along each

filament, transforming it to another helical form. This helix will then rotate. It seems that no macroscopic material has the ability to switch handedness in this way, so we must look to numerical simulation (or theory) to examine this phenomenon. The interaction between the material properties of the flagellum and the fluid dynamics is particularly intriguing.

Recently, it has become possible to label the flagella on a cell with a fluorescent marker molecule, permitting amazing visualisation of the whole run and tumble process and the transitions of flagella from one helical state to another [16]. This exciting discovery enables a closer examination of what flagella are actually doing during the bundling-unbundling transitions, should shed some light upon the three questions given.

1.2. Flagellar structure and polymorphism

A useful review paper detailing the construction of bacterial flagella is [5].

The flagellum begins at the rotor of the bacterial flagellar motor. Attached to the rotor is a drive shaft, called the rod, which is held in place by a bushing embedded in the outer membrane of the cell wall. Just outside the bushing, there is a short, highly curved segment called the hook. It has length 50nm and diameter 20nm, and is made from a special hook protein. The hook is observed to be quite flexible and is therefore assumed to take on the role of a universal joint, permitting the motor torque to be transmitted to the main part of the filament over a wide range of directions. It must therefore be an interesting object in its own right, having a high torsional rigidity (to transfer torque) but low bending rigidity. The propeller itself is a long, homogeneous filament of diameter 23nm and length up to about $15\mu\text{m}$, and is constructed entirely of the protein flagellin. This protein polymerises into 11 protofilaments, forming a tube which is coiled as the observed cell-scale helix. Finally, at the distal end of the flagellum there is a short cap structure which is believed to be responsible

for the correct assembly of the filament during growth. During growth, flagellin monomers pass down the interior of the filament tube and join on to the end of the filament. The cap may act as a chaperone (causing the monomers to take on the correct conformation to join the filament more quickly) or may simply prevent them from escaping (in view of the fact that flagellin polymerises successfully in solution without the cap proteins) [17].

We shall be concerned with the mechanics of flagellar polymorphism. A complete description of the protein-scale details of polymorphism (as known to date), however, is beyond the scope of this dissertation, and not specially relevant to modelling Hotani's experiments. It will be sufficient to state the following few facts.

Different polymorphic states have been observed in nature using strains of *Salmonella* bacteria. During swimming as described above the left-handed state is called the *normal* and it interchanges with a right-handed state, which may be *curly* or *semi-coiled*. The normal state is a helix of pitch $2.30\mu\text{m}$ and radius $0.45\mu\text{m}$. The curly state has pitch $1.14\mu\text{m}$ and radius $0.30\mu\text{m}$. The semi-coiled state has pitch $1.24\mu\text{m}$ and radius $0.52\mu\text{m}$. Several other polymorphic states have also been observed in different situations.

In three papers from 1975-1977, Calladine [18] provided a theoretical explanation for the different structures observed. He assumed that each monomer can take on two different conformations of slightly different size and shape and that each flagellin protofilament is built using only a single conformation. The lengths per monomer of the two different protofilament types therefore differ slightly. As neighbouring protofilaments need not be the same, one immediately sees how an intrinsic bend and twist can be built into the whole filament. By choosing different collections of protofilaments to make up the tube, he was able to propose a whole series of helices with different geometries and, by choosing the properties of the monomer bistability, fit the observed helical types. Calladine did not know that the flagellin monomer was bistable - this has only recently (2001) been proven through examination of the

crystal structure [19]. It is quite remarkable how well Calladine's analysis has been borne out by experiment.

1.3. The Hotani experiment

In a beautiful series of papers, Hotani [2] studied the properties of a single flagellum under mechanical stresses reminiscent of those it might undergo during natural swimming. The experimental protocol was as follows: a strain of *Salmonella* bacteria exhibiting purely normal flagella was cultivated and the flagella filaments were isolated and purified. These flagella were broken into smaller pieces, and then a small part was saved while the larger part was heated to break the filaments down into monomers. The retained smaller pieces were then mixed with the monomers to grow long filaments. The filaments were then observed using dark-field microscopy, and the observations recorded onto video.

In the 1979 paper Hotani observed flagella stuck to the glass slide by one of their ends. He then subjected the flagella to a steady shear flow (using a methylcellulose solution) of a few $\mu\text{m/s}$ and observed that they began to rotate about their axes. The 1982 paper concerns flagella which are stuck to the glass by a short segment near the end. These filaments were observed not to rotate, but the free portion of the filament could cyclically change its form to that of a different helix in a curious way, as presented in figures 1.2 and 1.3.

We begin with a helix of a single normal helical form. The flow is switched on, and causes a transformation (a "perversion") to a helix of opposite handedness (semi-coiled state) to occur near the stuck end. This region of the semi-coiled state invades the original state, growing until it reaches a certain length, when a transformation of the filament back to its original normal state occurs at the stuck end. The new region of the normal state invades the semi-coiled state and a cycle of nucleation, propagation and resetting of different helical forms occurs. One might say that a

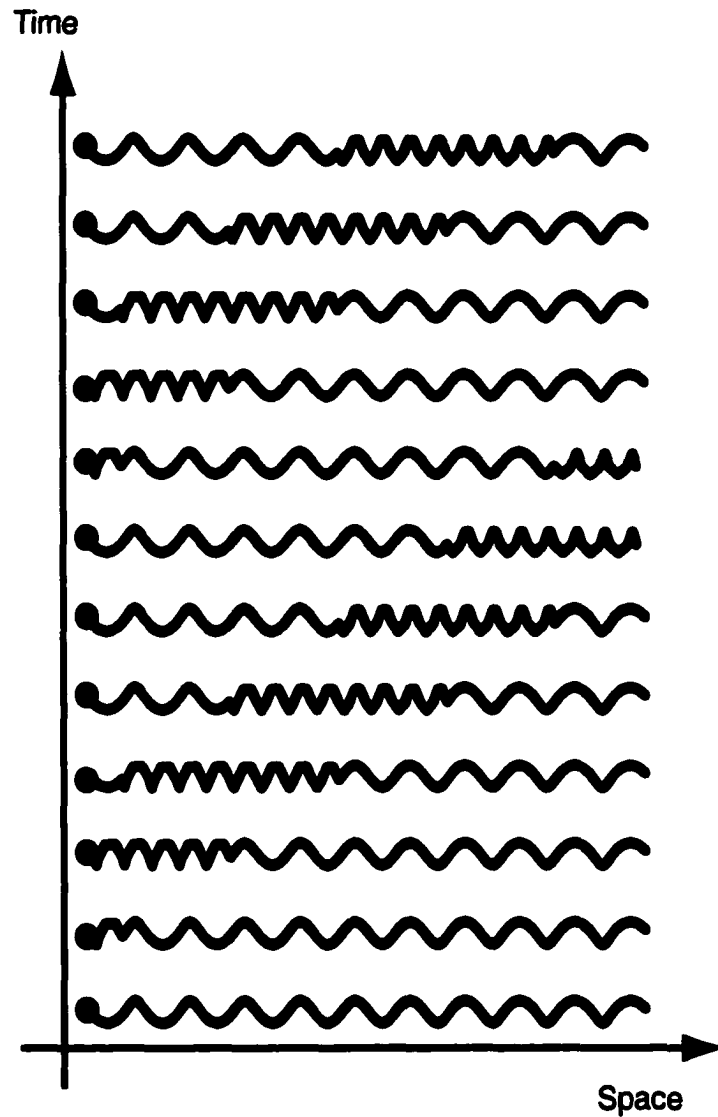


FIGURE 1.2. Schematic diagram of Hotani's results. This figure presents a time series of snapshots of a single flagellum, pinned at the left hand end under a uniform external flow to the right, viewed from above. Initially the flagellum is entirely left handed. Observe nucleation of a domain of a right-handed state at the pinned end. This domain grows until the pinned end resets to left-handed, then propagates with the flow and smoothly exits the filament, but not before a second nucleation event occurs at the pinned end. Nucleation, propagation and resetting then occur cyclically. Notice the shorter pitch of the right-handed state. The typical frequency of nucleation is 1-2 Hz.

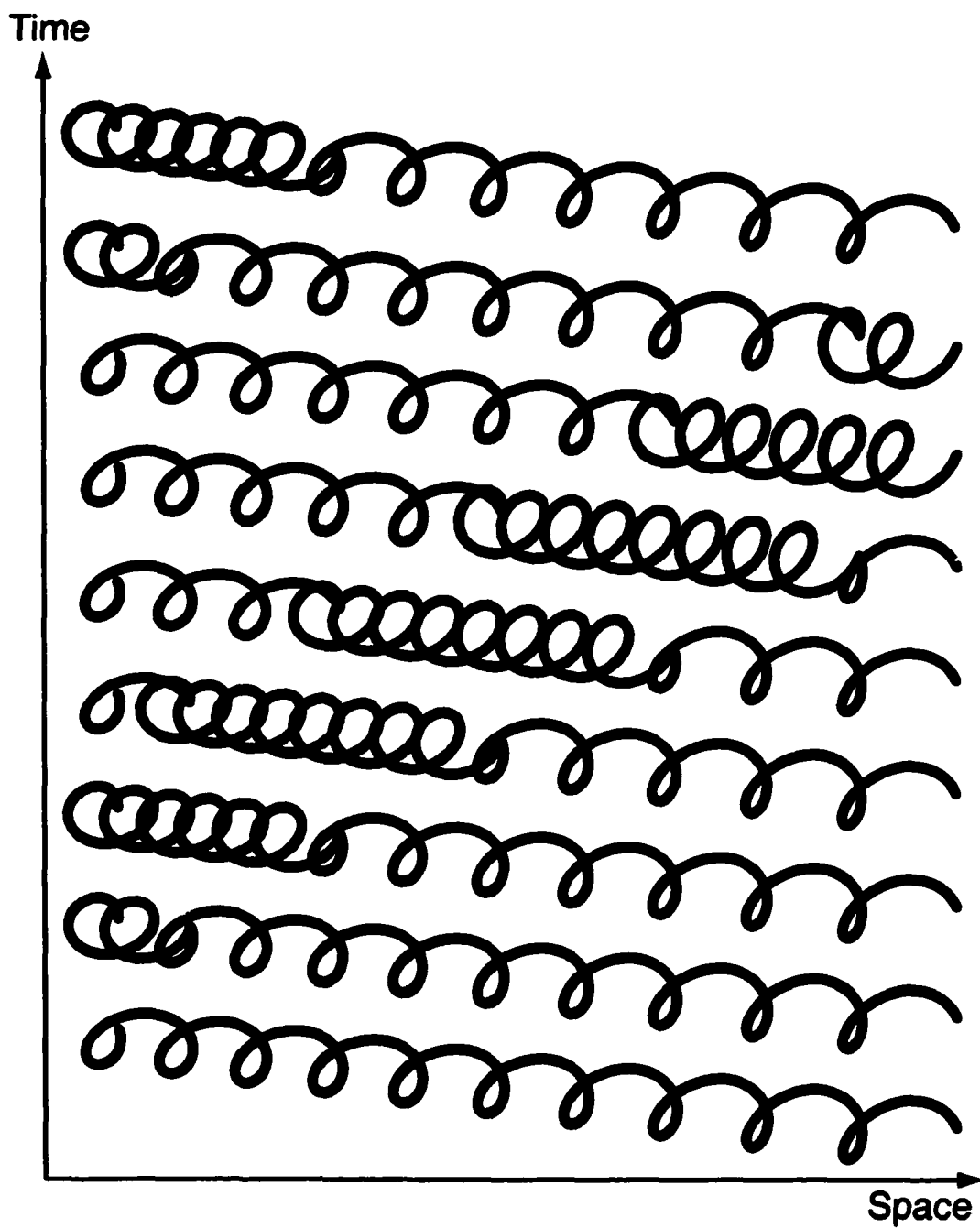


FIGURE 1.3. 3-dimensional diagram of Hotani's results. Here we present a three-quarter view of the filament, highlighting the handedness reversal. Each picture has an exact analogue in figure 1.2 and the left hand end is again pinned.

DC fluid flow is invoking an AC response from the helix, reminiscent in spirit of the Josephson effect in superconductivity [20].

This experiment clearly shows that mechanical forces can act to cause flagellar polymorphism. We expect by analogy that the mechanical forces acting on a flagellum during swimming, as described above, will cause the observed polymorphism there. This experiment forms by no means an exact simulation of those forces. During swimming, the helical filaments are forcing the bacterium forward and are therefore under a compressive force, whereas here they are under tension [21]. Also, the flow patterns near a peritrichously flagellated bacterium during swimming will be far more complex than those near a passive flagellum. However, this experiment remains, after nearly twenty years, the cleanest demonstration of the intrinsically nonlinear elasticity of flagella in a dynamic setting. A theory must be developed to explain it if we are to see a clear picture of the mechanics of bacterial swimming.

Our analysis, inspired by the work of Purcell [22] and the analysis of Hotani, begins with a careful examination of the torque acting on different parts of the filament (figure 1.4). Just as a rotating helix produces an axial fluid flow, so an axial fluid flow will generate a spatially-varying unwinding stress on a helix. Consider a filament that is entirely a left-handed helix. The fixed end experiences the greatest torque: it feels the torque due to flow past the entire helix. The free (downstream) end experiences no torque. Now imagine a filament consisting of two helices of opposing handedness spliced together. The net torque on the fixed end, by cancellation of opposing torques, is close to zero. We observe that, to a good approximation, rotary stress on the fixed end of the filament is specified entirely by the downstream configuration of the filament, and cycles from positive to negative as pulses of oppositely handed helices progress down the filament. It thus appears that the nucleation of a polymorphic region at the fixed end occurs as a response to this torque.

As described above, it is known that the flagellin monomers are intrinsically bistable themselves. We therefore picture the mechanically induced alteration of

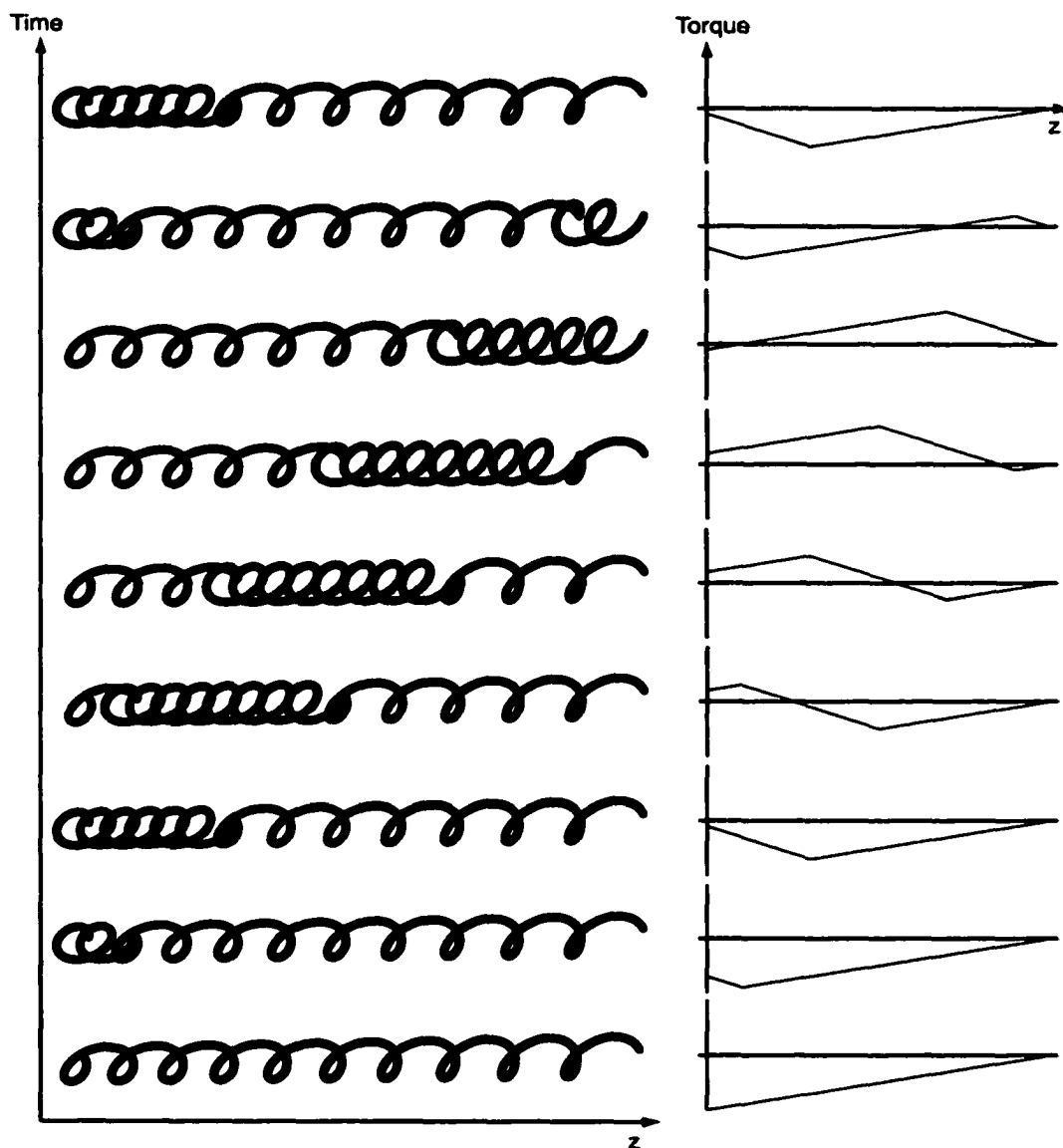


FIGURE 1.4. Illustration of torque experienced at different points along concatenated helices. We reproduce the filaments from figure 1.3 along with corresponding plots of the torque as a function of z due to a uniform flow along the helical centreline. The torque at the free end is always zero. Upstream torques are essentially integrals of some local 'helicity' function.

many individual monomers (and so rearrangement of the strand packing structure) at the nanometer scale leading to a new helical structure of the flagellum at the micron scale.

1.4. Discussion

This dissertation describes an extension of the normal linear elasticity theory for filaments to the case of a bacterial flagellum, as initially proposed (without external flow) in [23]. The extension is to permit the flagellum to have two stable states corresponding to helices of opposing handedness. We describe the bistability in the continuum sense, that is, we make no attempt to model the underlying motions of proteins. This might be thought of as a kind of spatial averaging over unimportant details in order to model the system on the length scales of interest. Having described the elastic energy of the flagellum, we generate dynamical equations to describe the evolution of its shape and twist profile in time, under the kind of fluid forcing present in Hotani's experiment. The major result is that, using real, experimentally determined parameters, we obtain *quantitative* agreement with the Hotani experiments. This is the first justification of the use of a bistable twist energy in modeling flagella, and it suggests very strongly that the model captures the essential physical features of the system.

The work presented here lies within the general field of *elastohydrodynamics* [24], the study of the dynamics of elastic (and mostly tiny) objects immersed in viscous fluids. The interest in this field has been stimulated almost entirely by biological questions. Some examples are (as described above) the swimming of organisms such as sperm and bacteria [25], the deformations required of red blood cells to travel down capillary vessels [26] and the beating of the heart [27]. In each case the defining questions are the same: how does the fluid deform the elastic object, and conversely how does the presence of the moving object affect the fluid flow? Each problem demands a different emphasis - the interest may lie more within the fluid-dynamics or

the elasticity theory. (This dissertation falls into the second category. We shall reduce the fluid interaction to a simple uniform forcing, but spend a long time developing elasticity.)

The initial inspiration for this work came from asking the three questions posed regarding bacterial swimming in section 1.1. It seems that to begin to analyse these questions, we have to understand the elasticity of bacterial flagella. The Hotani experiment is not a perfect simulation of swimming by any means. It is possible that a future experiment might reveal some interesting complexities - for instance, the existence of important correlations between (say) extensive force and twist elasticity. This kind of discovery would be a natural extension of the model presented here. We therefore believe that our theory explaining the Hotani experiment will be a valuable tool for theorists examining any of the three questions posed.

In the preceding section, we gave a general description of the behaviour of a flagellum under an axial fluid stress. Our strategy is now as follows. Chapter 2 translates the basic mechanics of the Hotani experiment into the language of the elasticity theory of thin rods, ultimately leading to partial differential equations which describe the experiments. These equations are themselves interesting mathematical objects and are amenable to some analysis, presented in Chapter 3. Finally in Chapter 4 we discuss the numerical methods used in simulating the experiment, and present the results.

2. MODEL

In order to develop a physical model to substantiate the ideas of torque - based polymorphism given in section 1.3, we recast the Hotani experiment into the language of the elasticity theory of thin rods. This chapter begins with a discussion of that theory for a simple, naturally straight and untwisted elastic rod. In particular we are concerned with the dynamics of elastic relaxation of such a rod in a viscous fluid. We then generalise to the case of an intrinsically bent and twisted rods, finally developing the model to describe filaments with two stable helical configurations. Balancing the elastic force with fluid drag forces gives us a description of Hotani's experiment in terms of two coupled, nonlinear partial differential equations. The chapter ends with some simple analysis of the system and discussion of the important dimensionless parameters in the problem.

2.1. Elasticity of thin rods

The classic derivations of the usual elasticity model for a homogeneous thin rod are found in Love [28] and Landau and Lifshitz [29]. The latter is more accessible to the modern reader, and follows (to my mind) a more natural progression. This discussion begins with an examination of the popular geometrical Frenet-Serret frame for filaments. We then move to a more natural set of coordinates and develop the overdamped dynamics that will be used to model the Hotani experiment.

Mathematically the position of a filament may be described in a variety of ways. The simplest is to think of the filament centreline as a parameterised curve

$$\mathbf{r}(s) = (x(s), y(s), z(s)) \quad (2.1)$$

in three-dimensional space, where s , the arc length parameter, runs from say 0 to L , the length of the filament. Throughout this discussion we will consider inextensible

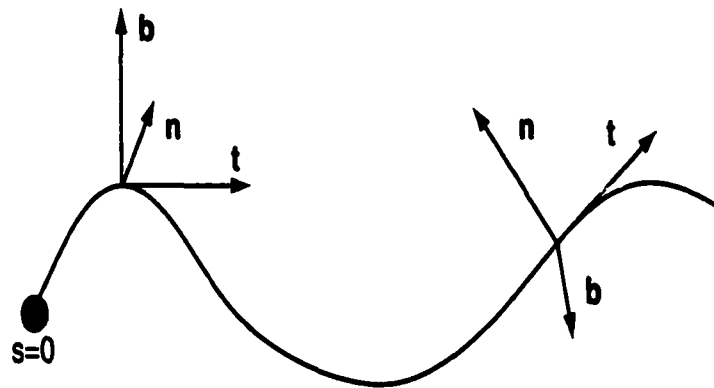


FIGURE 2.1. Frenet-Serret frame. \mathbf{t} is the unit tangent, \mathbf{n} points along the direction of maximum curvature and \mathbf{b} makes up an orthonormal basis at each point along the curve.

rods only, so L is constant. This is an external, fixed frame. Given that the elastic energy of an object is independent of its position in space, but depends strongly on how it is deformed internally, it is more natural to develop our ideas in *intrinsic* coordinates.

The classic intrinsic description of a filament is the Frenet-Serret frame [30]. Away from corners, we define the *tangent* vector of the curve,

$$\mathbf{t}(s) = \mathbf{r}'(s). \quad (2.2)$$

The important geometric quantity of the *curvature* is now defined as the rate of turn of $\mathbf{t}(s)$ with respect to s , $\kappa = |\mathbf{t} \times \mathbf{t}'|$. \mathbf{t} turns instantaneously about the vector $\mathbf{t} \times \mathbf{t}'$. Using this, we distinguish two perpendicular normal vectors to \mathbf{r} at any point of non-zero curvature. The unit *normal* vector \mathbf{n} is defined by $\mathbf{t}' = \kappa \mathbf{n}$ and points, therefore, in the direction of the turn of \mathbf{t} (perpendicular to \mathbf{t}). The unit *binormal* vector \mathbf{b} forms an orthogonal triad together with \mathbf{t} and \mathbf{n} (and points in the direction of $\mathbf{t} \times \mathbf{t}' = \kappa \mathbf{t} \times \mathbf{n}$). Note the natural geometric interpretation of κ - it is the inverse radius of a circle inscribed tangent to the filament at a point.

Observe that the $\mathbf{n} - \mathbf{b}$ axes will rotate as s varies. Thus, we define the geometric

torsion of the curve by $\mathbf{b}' = -\tau\mathbf{n}$, so τ is the rate at which \mathbf{b} rotates away from \mathbf{n} . This leads to the famous Frenet-Serret equations:

$$\begin{pmatrix} \mathbf{t}' \\ \mathbf{n}' \\ \mathbf{b}' \end{pmatrix} = \begin{pmatrix} 0 & \kappa & 0 \\ -\kappa & 0 & \tau \\ 0 & -\tau & 0 \end{pmatrix} \begin{pmatrix} \mathbf{t} \\ \mathbf{n} \\ \mathbf{b} \end{pmatrix} \quad (2.3)$$

We shall define a *helix* using this frame to be a line for which κ and τ are constant.

Note that the curvature and torsion in the Frenet-Serret description are geometric properties. If we consider a physical elastic filament, it is obvious that it may be physically twisted in a manner entirely inconsistent with its geometric torsion. We also notice that in regions of a curve that are straight ($\mathbf{t}' = 0$ on an interval) the normal and binormal vectors are undefined. In particular, at an inflection point ($\mathbf{t}'(s) = 0$, $\mathbf{t}''(s) > 0$ say), \mathbf{n} has a jump discontinuity as the $(\mathbf{t}, \mathbf{n}, \mathbf{b})$ frame rotates 180° instantaneously. Bearing these points in mind, we therefore reject the Frenet-Serret frame as a good choice for analysis of a physical elastic filament. We will try instead to define a coordinate system which reflects the actual bending of the material of the filament.

We begin by defining a coordinate system $\mathbf{e} = (\mathbf{e}_1, \mathbf{e}_2, \mathbf{e}_3)$ at each point along the filament centreline. We let $\mathbf{e}_3 = \mathbf{t}$, the unit tangent vector described above. \mathbf{e}_1 and \mathbf{e}_2 will complete the local orthonormal system, but will be related to physical properties of the filament. Temporarily, we can imagine a painted stripe on the side of the filament towards which \mathbf{e}_2 will always point. \mathbf{e}_1 completes a right handed triad. Then, if we bend or twist the filament, it is easy to picture the coordinate frame moving so that \mathbf{e}_1 remains tangent, and \mathbf{e}_2 remains pointed towards the stripe. See figure 2.2. Now define the vector $\Phi(s)$ as the angles of rotation of the system $(\mathbf{e}_1, \mathbf{e}_2, \mathbf{e}_3)$ around some fixed frame of reference, at the point $\mathbf{r}(s)$. Any smooth deformation of the filament is now described by

$$\Omega(s) = (\Omega_1(s), \Omega_2(s), \Omega_3(s)) = \frac{d\Phi}{ds}. \quad (2.4)$$

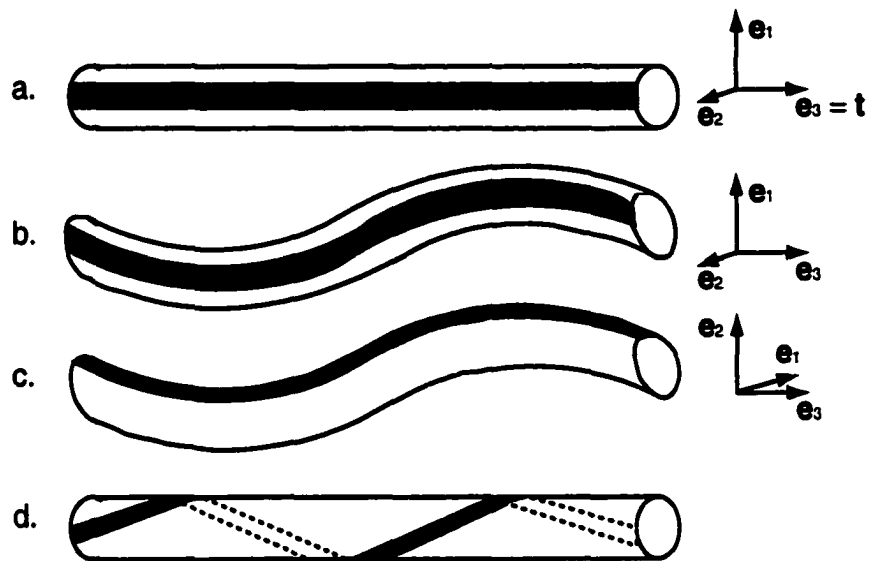


FIGURE 2.2. Natural frame. a. shows a filament with a stripe in a straight, untwisted state. b. shows curvature perpendicular to the stripe, that is, around the local e_2 axis. Similarly, c. shows curvature around the local e_1 axis and d., twist around the tangent (e_3) axis.

Ω measures the rate of rotation of the \mathbf{e} frame:

$$\frac{\partial \mathbf{e}_i}{\partial s} = \Omega \times \mathbf{e}_i. \quad (2.5)$$

Specifically, $\Omega_3(s)$ is the rate of rotation of the stripe around the filament centreline, $\Omega_1(s)$ measures bending in the plane containing the stripe, and $\Omega_2(s)$, bending in the direction perpendicular to the stripe (see figure 2.2). We will henceforth write Ω for Ω_3 as the twist rate. This description of the filament is sufficient for any differentiable configuration \mathbf{r} with differentiable twist information (stripe), and includes information about the physical twist state. $\Omega_1^2 + \Omega_2^2 = \kappa^2$, the Frenet-Serret curvature of the filament described above [29].

Assuming that the filament is slightly deformed, the elastic energy per unit length will be a quadratic function of the deformation vector Ω [29]. For our purposes we need only consider the case of a rod of circular cross-section and uniform composition. The elastic energy will therefore be invariant under $s \rightarrow -s$, ruling out twist-bend

Filament Configuration	Ω_1	Ω_2	Ω
Straight line	0	0	0
Circle of radius R	0	$\frac{1}{R}$	0
Helix of radius R and pitch P	0	$((2\pi)^2 R)/P^2$	$2\pi/P$

TABLE 2.1. Description of filament configurations in intrinsic frame

energy terms of the form $\Omega_1\Omega$ and $\Omega_2\Omega$ (although this need not be true for filaments with more complicated symmetries, for example DNA [31]). Bend-bend coupling terms of the form $\Omega_1\Omega_2$ are also precluded by these assumptions. The linear elastic energy of a thin rod with circular section is therefore given by

$$E = \int_0^L \left\{ \frac{A}{2} (\Omega_1^2 + \Omega_2^2) + \frac{C}{2} \Omega^2 \right\} ds. \quad (2.6)$$

The bending rigidity $A = E\pi R^4/4$ (of a solid rod) and twist modulus $C = \frac{1}{2}\mu\pi R^4$ are determined by material properties of the filament: the Young modulus E , modulus of rigidity μ and radius R [29]. We note that the bending rigidity for a tube of inner radius r is proportional to $(R^4 - r^4)$. In particular, flagella are tubes, but this is of little concern as the experiments we shall refer to for our estimate of the flagellar bending rigidity measure A directly.

An important approximation to the energy given above occurs in the case that the rod is approximately straight. We will use the coordinate system (x, y, z) where the undeformed filament is aligned with the z -axis. The position of the filament is now written as the triad $(X(z), Y(z), z)$. We will also let $\theta(z)$ be the angle through which the material frame has been twisted as a function of z . For brevity, we will sometimes adopt the convention that $\xi(z) = X(z) + iY(z)$, so the filament configuration is completely determined by the complex function ξ and the real function θ .

The vector $\mathbf{t} = \mathbf{e}_3$ is now approximately parallel to the z -axis. Therefore

$$\frac{d\mathbf{t}}{ds} = \frac{d^2\mathbf{r}}{ds^2} \simeq \frac{d^2\mathbf{r}}{dz^2} \quad (2.7)$$

and so

$$\Omega_1 \simeq -\frac{d^2 Y}{dz^2} = -\text{Im}[\xi_{zz}] \quad (2.8)$$

$$\Omega_2 \simeq \frac{d^2 X}{dz^2} = \text{Re}[\xi_{zz}]. \quad (2.9)$$

The bending energy is now approximated as

$$E_{\text{bend}} = \int_0^L \frac{A}{2} \kappa^2 ds \simeq \int_0^L \frac{A}{2} \left(\left(\frac{d^2 Y}{dz^2} \right)^2 + \left(\frac{d^2 X}{dz^2} \right)^2 \right) ds. \quad (2.10)$$

What is the error of this approximation? Considering the two-dimensional problem momentarily, we think about replacing $\mathbf{r}(s)$ (now a 2-vector) with some function $y(z)$ in the plane. We find [30] that

$$\kappa^2 = \frac{y_{zz}^2}{(1 + y_z^2)^3}. \quad (2.11)$$

Supposing that y_z is small, we can approximate this by

$$\kappa^2 \simeq y_{zz}^2 (1 - 3y_z^2 + O(y_z^4)). \quad (2.12)$$

Therefore, this approximation omits terms of order y_z^2 (also see the discussion on page 40). If we now suppose the filament is immersed in a fluid and the Reynolds number [32] is sufficiently low that inertia may be neglected, we may derive the damped beam equation (extensively studied in [33]) by balancing the variational derivative of E (representing the elastic restoring force) with the local velocity of the filament multiplied by a drag coefficient ζ_{\perp} (this is discussed further below).

$$\zeta_{\perp} \xi_t = -\frac{\delta E}{\delta \xi} = -A \xi_{zzzz} \quad (2.13)$$

In the process of differentiating E we must specify boundary conditions. Let us consider (most similarly to the Hotani experiment) a fixed, hinged end at $z = 0$: $\xi(0) = \xi_{zz}(0) = 0$ and a free end at $z = L$: $\xi_{zz}(L) = \xi_{zzz}(L) = 0$.

We rescale z by L and t by the time scale for the problem, $L^4\zeta_{\perp}/A$, commonly called the elastohydrodynamic diffusion time. Following this rescaling, we have $\xi_t = -\xi_{xxxx}$ with boundary conditions $\xi(0) = \xi_{xx}(0) = \xi_{xx}(1) = \xi_{xxx}(1) = 0$.

We will use a spectral approach to solving this problem. Define $L = \frac{\partial^4}{\partial x^4}$ acting on sufficiently differentiable functions in $L^2[0, 1]$ with the given boundary conditions. The null space consists of linear functions, and L 's eigenfunctions will be linear combinations of \sin, \cos, \sinh and \cosh functions. The fixed boundary condition at $x = 0$ removes cosine and cosh, and a brief calculation shows that the (unnormalised) eigenfunctions have the form

$$W_k = \frac{\sinh k}{\sin k} \sin kx + \sinh kx \quad (2.14)$$

where the k -values are the solutions of the transcendental equation

$$\tan k = \tanh k. \quad (2.15)$$

For large k these are approximately the solutions of $\tan k = 1$, so $k \simeq (2n + 1)\pi/4$ for positive integer n (note that this prevents the bad possibility $\sin k = 0$). When normalised, the corresponding large k eigenfunctions look very much like a sine basis. $k = 0$ corresponds to the null space of linear functions, which we ignore here. L is self-adjoint and therefore its eigenfunctions form an orthogonal basis for the function space in question. Therefore, given an initial configuration $\xi(0)$ we can exactly compute future configurations $\xi(t)$ by the following Fourier-type method. Begin by computing the set of projections

$$\xi_k = \int_0^1 \bar{W}_k \xi(t) dx \quad (2.16)$$

($\xi = \sum_k \xi_k \bar{W}_k$ where \bar{W}_k are normalised) to decouple the system into modes ξ_k . Then

$$\xi_t = \sum_k \frac{\partial \xi_k}{\partial t} \bar{W}_k = -\xi_{xxxx} = -\sum_k k^4 \xi_k \bar{W}_k. \quad (2.17)$$

Integrating in time,

$$\xi(t) = \sum_k e^{-k^4 t} \xi_k(0). \quad (2.18)$$

In other words, all frequencies are damped extremely quickly, leaving only the projection of the zero eigenfunction onto $\xi(0)$. We might say the bends *hyperdiffuse* away to leave the straight, preferred state [33].

We now look at the damped dynamics of a filament which is straight but twisted around its axis ($\Omega_1 = \Omega_2 = 0$). If the filament has a straight painted red stripe on one side in equilibrium, then as it is twisted, it will take on the appearance of a twisted stick of striped “Brighton Rock” or a straight candy cane (depending on your perspective). We will again suppose the filament is submerged in a viscous medium and balance the elastic restoring torque (the functional derivative of E) with a viscous drag coefficient times an angular velocity. Also, suppose the filament is aligned with the z -axis. First, write the twisting energy in terms of θ (where $\Omega = \theta_z$ in this approximation) as follows,

$$E_{twist} = \int_0^L \frac{C}{2} \Omega^2 dz \int_0^L \frac{C}{2} \theta_z^2 dz \quad (2.19)$$

Now perform the torque balance to obtain

$$\zeta_R \theta_t = C \theta_{zz} = C \Omega_z \quad (2.20)$$

which is just a diffusion equation for twist. ζ_R is the rotational drag coefficient. Physically, this equation makes sense: a twisted rod will want to move only if the twisting strain Ω varies from point to point, so the torque must vary with Ω_z . Rescaling by the filament length L , we see that the characteristic time scale for twist diffusion is given by $\zeta_R L^2 / C$. Comparing to the bend diffusion time $L^4 \zeta_{\perp} / A$, we immediately realise that for a long filament the twist dynamics will be far quicker than the bend dynamics, due to the relative powers of L . The same is true for shorter filaments, for $\zeta_R \simeq 10^{-13}$ is many orders of magnitude smaller than $\zeta_{\perp} \simeq 1$ (see section 2.4). For

a general filament of Young's modulus E , modulus of rigidity μ and radius R , the bending modulus A scales as ER^4 while C scales as μR^4 (see page 26). Therefore, for a material of remotely comparable Young modulus and modulus of rigidity, short filaments will experience twist diffusion more quickly than bend hyperdiffusion.

The rescaled equation $u_t = u_{xx}$ is easily solved by a projection method, exactly analogously to the damped beam equation described above. If we consider the boundary conditions that the filament is irrotationally fixed at one end ($u(0) = 0$) and free at the other end ($u_x(1) = 0$) we obtain a sine basis, each mode of which is damped (as is usual for the heat equation) by a factor like $e^{-k^2 t}$ over time. For this equation there is no zero eigenfunction so any imposed filament twist will just diffuse away.

In the above discussion of elastic relaxation we have assumed that the only effect of the fluid is to provide resistance to motion, and modeled that resistance with a local drag coefficient. This assumption is a considerable simplification! We will be concerned with modeling the Hotani experiment with the flagellum of a bacterium (scale L) moving at speeds U of at most $\sim 10\mu\text{m/s}$ in a solution of methylcellulose¹ of kinematic viscosity $\nu \sim 1$. The relevant Reynolds number, UL/ν is therefore of order $10^{-3}10^{-3}/1 = 10^{-6}$ at the most (taking the length scale to be the length of the flagellum). This tells us that inertial effects can be altogether neglected and the fluid dynamics will be governed by the incompressible Stokes equations,

$$\mathbf{u}_t = \nu \nabla^2 \mathbf{u} \quad (2.21)$$

$$\nabla \cdot \mathbf{u} = 0. \quad (2.22)$$

(where \mathbf{u} is the velocity of the fluid.) In this regime forces balance velocities - we are at the Aristotelian limit.

The local resistance per unit length of an infinitely long slender body of diameter d and length L to normal motion is calculated [37] to be

$$\zeta_{\perp} = \frac{4\pi\mu}{\ln(L/d) + c} \quad (2.23)$$

¹we ignore any non-Newtonian properties of the fluid

where c is an order one constant depending on the exact shape of the body. The tangential resistance coefficient for such a body is $\zeta_{\parallel} \simeq \zeta_{\perp}/2$. Similarly we can compute the resistance to rotation (per unit length) of a slender cylinder,

$$\zeta_R = 4\pi\mu(d/2)^2. \quad (2.24)$$

These calculations are made in idealised situations. In the case of the moving bacterial flagellum, it is obvious that the filament itself will move the fluid significantly and there will be non-local coupling between different parts of the filament. We choose to neglect this effect and replace the fluid with local resistance coefficients. This choice significantly simplifies matters, and provides us with a simple test-bed to examine the physics of elasticity of flagella, which is the less-studied and more interesting aspect of the problem.

We now consider the case of a filament with an intrinsic constant curvature bend (if it is long enough, such an object forms a circular loop in its unstressed state). Assume that this bend is entirely in the Ω_2 plane and has curvature Ω_2^0 . The bending energy of this filament will be

$$E_{bend} = \int_0^L \frac{A}{2} (\Omega_1^2 + (\Omega_2 - \Omega_2^0)^2) ds. \quad (2.25)$$

It is not correct to make the linearisation (2.7) given above for this rod unless the length L is much less than the radius of curvature $1/\Omega_2^0$. However, we may write $\hat{\Omega}_2 = \Omega_2 - \Omega_2^0$ and then linearise the resulting energy about the minimum energy state $\Omega_1 = \hat{\Omega}_2 = 0$. Immersing the filament in a viscous fluid, we obtain the damped beam equation again for perturbations around the steady state - perturbation modes are again damped as $\partial u_k / \partial t = -k^4 u_k$.

Suppose we now permit the energy of a purely torsional deformation of a straight rod to be

$$\int_0^L V(\Omega) dz = \int_0^L V(\theta_z) dz. \quad (2.26)$$

The naturally untwisted rod above has $V(\Omega) = (C/2)\Omega^2$. Functionally differentiating this, and equating the resulting torque to the angular drag, we find the overdamped dynamical equation

$$\zeta_R \theta_t = \theta_{zz} V''(\theta_z) = (V'(\theta_z))_z = (V'(\Omega))_z. \quad (2.27)$$

We are now considering a *non-linear* constitutive relationship between stress and strain in the filament, described by the function V . Torques are now generated by spatial variations in $V'(\Omega)$ (dimensionally, $V'(\Omega)$ has units of energy, or torque, so spatial variations generate a force). Consider a naturally twisted rod with a preferred twist rate of $2\pi/P$ (thinking of P as the pitch with which our painted stripe rotates around this particular piece of candy-cane). We then have $V(\Omega) = (C/2)(\Omega - (2\pi/P))^2$ where C bears a strong resemblance to the twist modulus, at least for large P . The dynamics are given by

$$\zeta_R \theta_t = C \theta_{ss} \quad (2.28)$$

exactly as for the filament which prefers to be untwisted. The difference lies in the boundary conditions. A filament with twist potential V that is irrotationally clamped at $s = 0$ but free at $s = L$ will have natural boundary conditions $\theta(0) = 0$ and $V'(\theta_z(L)) = 0$. So we immediately see that new twist may only enter the system from the free end. Away from the end, twist simply diffuses. Another way of saying this is that the dynamics form a conservation law away from the free end (which allows twist flux to enter or leave the system).

Rescaling by L and the twist diffusion time, we are left with the problem of solving $\theta_t = \theta_{xx}$ subject to $\theta(0) = 0$ and $\theta_x(1) = K \equiv 2\pi L/P$ with initial configuration θ_0 . The simplest way to do this is by letting $\theta = \hat{\theta} + Kx$. Then we are returned to the problem $\hat{\theta}_t = \hat{\theta}_{xx}$ with $\hat{\theta}(0) = 0$ and $\hat{\theta}_x(1) = 0$. The filament ultimately relaxes to its preferred twist state exactly as before.

A filament with a natural bend (Ω_2^0 , say) and twist (pitch $2\pi/P$) will relax to a

helical state. We may write the elastic energy as

$$E = \int_0^L \left\{ \frac{A}{2} (\Omega_1^2 + (\Omega_2 - \Omega_2^0)^2) + \frac{C}{2} \left(\Omega - \frac{2\pi}{P} \right)^2 \right\} ds. \quad (2.29)$$

Drawing on the previous few sections, we see that we may choose new variables $\hat{\Omega}_2 = \Omega_2 - \Omega_2^0$, $\hat{\Omega}_3 = \Omega - 2\pi/P$ and then linearise deformations about the preferred helical state. To the same order in X_z, Y_z we may also simply insert linearised approximations for Ω_1, Ω_2 into the energy. The material frame now rotates with $\theta(z)$ and so the linear strain approximations are rotated appropriately to

$$\Omega_1 = -\frac{\partial^2 Y}{\partial z^2} \cos \theta + \frac{\partial^2 X}{\partial z^2} \sin \theta = -\text{Im}(\xi_{zz} e^{-i\theta}) \quad (2.30)$$

$$\Omega_2 = \frac{\partial^2 X}{\partial z^2} \cos \theta + \frac{\partial^2 Y}{\partial z^2} \sin \theta = \text{Re}(\xi_{zz} e^{-i\theta}) \quad (2.31)$$

$$\Omega_3 = \frac{\partial \theta}{\partial z}. \quad (2.32)$$

We can now generate overdamped dynamics for the helix by functional differentiation and balance of forces with drags:

$$\zeta_{\perp} \xi_t = -A (\xi_{zz} - \Omega_2^0 e^{i\theta})_{zz} \quad (2.33)$$

$$\zeta_R \theta_t = \frac{C}{2} \theta_{zz} - A \Omega_2^0 \text{Im}(\xi_{zz}^* e^{i\theta}) \quad (2.34)$$

Recalling the importance of boundary conditions from the previous examples, we note them here for the relevant case of a filament irrotationally fixed at one end and free at the other:

$$\xi(0) = \theta(0) = \theta_{zz} = 0, \quad \xi_{zz}(0) = \Omega_2^0, \quad (2.35)$$

$$\xi_{zz}(L) = \Omega_2^0 e^{i\theta}, \quad \xi_{zzz}(L) = (\Omega_2^0 e^{i\theta})_z, \quad \theta_{zz}(L) = 0, \quad \theta_z(L) = \frac{2\pi}{P} \quad (2.36)$$

where $e^{i\theta}$ and its derivatives are evaluated at $z = L$.

Examining the bend equation we see that it is an exact analogue of that for the filament with constant intrinsic bend. However, the term $\Omega_2^0 e^{i\theta}$ is dependent on z and t . The bend relaxation is thus towards a moving, non-constant target. The obvious

bend relaxation time scale of $\zeta_{\perp} L^4/A$ remains, but there are potentially new time and length scales brought to the problem from the twist equation via the $e^{i\theta}$ term. Supposing for a moment that θ is a fixed function, we obtain

$$\xi_t = -(\xi_{zz} - \Omega_2^0 e^{i\theta})_{zz} \quad (2.37)$$

with the given boundary conditions. If we define $\hat{\xi}$ so that $\hat{\xi}_{zz} = \xi_{zz} - \Omega_2^0 e^{i\theta}$ then we are immediately returned to the case

$$\hat{\xi}_t = -\hat{\xi}_{zzzz} \quad (2.38)$$

with the homogeneous boundary conditions described above. This tells us that ξ always relaxes towards the steady state $\xi_{zz} = \Omega_2^0 e^{i\theta}$ - when θ varies with time as well, the shape of the filament is relaxing towards a moving target. The twist equation is still of diffusion form but now contains an interesting (and nonlinear) forcing term. We note that if the bend equation is in equilibrium, so $\xi_{zz} = \Omega_2^0 e^{i\theta}$, then there is no forcing, for $\xi_{zz}^* e^{i\theta} = \Omega_2^0$ which is purely real. The energy minimising shape with these boundary conditions is the helix of radius $\Omega_2^0 (P/(2\pi))^2$ and pitch P ,

$$\xi = -\Omega_2^0 \left(\frac{P}{2\pi} \right)^2 e^{i\theta} + Mz, \quad \theta = \frac{2\pi z}{P} \quad (2.39)$$

where M is in principle undetermined. However, in order that the linear approximation to the strains is as nearly correct as possible (see equation (2.12)), M should be chosen so the filament runs as nearly as possible along the z -axis (generally, $M = 0$ will be a good choice). The main point to notice in (2.33) and (2.34) is the fact that it is possible for a twisting motion to relax a bending deformation, and vice-versa.

This discussion of basic filament dynamics is now generalised to the particular case of the Hotani experiment.

2.2. Derivation of the PDE model

The linear elasticity theory described above will not describe an object with two stable states. The observation that flagella support two stable helices of opposing

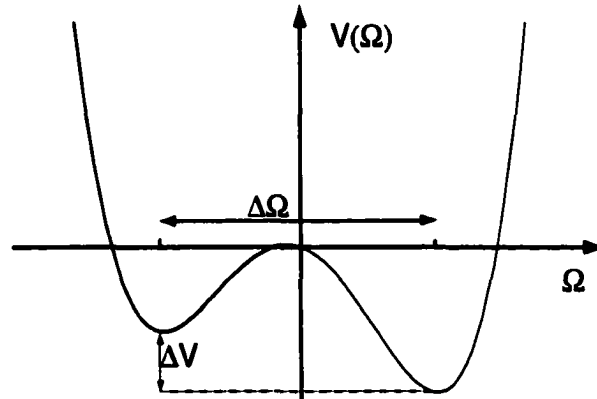


FIGURE 2.3. Bistable potential.

handedness can, however, be extended to include such objects. Helices of opposite handedness have twist rates (Ω) with opposing signs. We propose, following [23], to replace the singly stable twist energy $\frac{C}{2}(\Omega - \frac{2\pi}{P})^2$ with a bistable Landau potential $V(\Omega)$ which has two locally stable states (figure 2.3).

The exact details of the potential in principle can be elucidated from microscopic measurements. Local to the minima, the potential should reflect the shape of a singly stable energy function. Any analytic bistable potential will contain regions of negative concavity, where the damped candy-cane equation $\zeta_R \theta_t = V''(\theta_s) \theta_{ss}$ becomes antidiffusive. This means oscillations of all frequencies are amplified! Fortunately, and on a variety of grounds [34], we note that if two states of opposing handedness coexist there must be a finite width region in which they are smeared together. Primarily, the very general theory of inhomogeneous systems demands that two regions of different states may not meet without a transition region [34]. The width of the region will fluctuate about the mean at finite temperature. Secondly, geometry dictates the “block angle” between two perfect helices spliced together. When observing two flagellar helices spliced together, Hotani noted a systematic deviation from the predicted block angle. This was neatly explained in [23] by assuming a transition region

existed. We therefore introduce an energetic cost for twist-front gradients controlled by a parameter γ , to end up with

$$E_{twist} = \int_0^L \left\{ V(\Omega) + \frac{\gamma^2}{2} \Omega_s^2 \right\} ds \quad (2.40)$$

The candy-cane equation now contains a hyperdiffusive piece:

$$\zeta_R \theta_t = -\gamma^2 \theta_{ssss} + V''(\theta_s) \theta_{ss} = (-\gamma^2 \theta_{sss} + V''(\theta_s))_s \quad (2.41)$$

The dispersion relation for this equation (obtained by replacing θ by a Fourier component $e^{\lambda t} e^{iks}$) is now

$$\lambda = -k^4 + \dots \quad (2.42)$$

so high frequency oscillations scaling with $-k^2$ are seen to be damped.

Generally speaking, V'' will be a nonlinear function. A full examination of the candy-cane twist equation will be completed in the next chapter, however for now we can note that it supports simple solutions of the form $\theta = Rz$ where R can be any solution of $V'(x) = 0$. We also expect tanh-like front solutions corresponding to connections between solutions $\theta = R_0 z$ and $\theta = R_1 z$ where $R_{1,2}$ are minima of V .

We might also consider a non-analytic potential function of two quadratic pieces spliced together. In that case, the candy-cane equation becomes $\zeta_R \theta_t = -\gamma^2 \theta_{ssss} + M \theta_{ss}$ where M takes two values depending on the local value of θ_s . This case is also considered further in Chapter 3.

Our extension of elasticity to include bistable helices is essentially phenomenological. In principle all the preceding theory should be derived as the continuum limit of a few simple assumptions governing the interactions of individual molecules [35].

The two helices taken on by flagella in Hotani's experiments have different intrinsic curvatures. Note that we have made a simplification by taking these to have the same value, Ω_2^0 , which is definitely not the case for real flagella. However, we believe the general features of the experiment will remain.

The total energy of our bistable helix, as described above, is now given by

$$E = \int_0^L \left(\frac{A}{2}(\Omega_1^2 + (\Omega_2 - \Omega_2^0)^2) + V(\Omega) + \frac{\gamma^2}{2}\Omega_z^2 \right) dz \quad (2.43)$$

We generate an elastic force by functionally differentiating the energy and balance this force and torque with a drag on the filament motion, as described above.

$$\zeta_{\perp}\xi_t = -A(\xi_{zz} - \Omega_2^0 e^{i\theta})_{zz} \quad (2.44)$$

$$\zeta_R\theta_t = -A\text{Im}(\Omega_2^0 \xi_{zz}^* e^{i\theta}) - \gamma^2\theta_{zzzz} + \theta_{zz}V''(\theta_z) \quad (2.45)$$

These equations, first derived without linearisation in [23], describe the overdamped elastic relaxation of a filament with preferred curvature Ω_2^0 and twist energy given by $V(\theta_z)$.

In the process of functionally differentiating we find the natural boundary conditions. The filament is clamped irrotationally at the left hand ($z = 0$) end but is free at the right hand end:

$$\begin{aligned} \xi(0) = 0, \quad \xi_{zz}(0) = \Omega_2^0, \quad \xi_{zz}(L) = \Omega_2^0 e^{i\theta(L)}, \quad \xi_{zzz}(L) = (\Omega_2^0 e^{i\theta(L)})_z \\ \theta(0) = 0, \quad \theta_{zz}(0) = 0, \quad \theta_{zz}(L) = 0, \quad \gamma^2\theta_{zzz}(L) = V'(\theta_z(L)) \end{aligned} \quad (2.46)$$

The final boundary condition, that the rod is torque-free at its free end, is significant in that it prevents the use of a pseudo-spectral method for solution of the twist equation. This will be fully discussed in Chapter 4.

With the natural boundary conditions, let us briefly consider the case of a rod with no intrinsic curvature. The bend and twist equations decouple and we are left with the overdamped beam equation, $\zeta_{\perp}\xi_t = -A\xi_{zzzz}$ and candy-cane twist equation $\zeta_R\theta_t = -\gamma^2\theta_{zzzz} + \theta_{zz}V''(\theta_z)$.

Having established the (linearised) equations governing the relaxation of a rod with intrinsic bend and a twist potential, we can now build in a fluid forcing term to simulate the Hotani experiment. Physically, there is a balance between the elastic force due to deformations and the drag force exerted by the fluid on the filament,

at each point along the filament. A full explanation would involve (probably numerically) immersing the elastic filament in a 3-dimensional moving fluid, and fully simulating the dynamics (via Navier-Stokes) of the filament acting on the fluid, and the fluid acting on the filament. Simulations similar to these (the ‘immersed boundary method’) have been performed in simple cases by Peskin, Fauci and collaborators [36]. We opt for a simpler approach that still captures the essence of the problem. The fluid will act to provide a simple drag force on the filament in the direction of the z -axis. It will also resist motion in the x and y directions, as discussed above. This simplification means that different parts of the filament cannot communicate via the fluid. Note that a cylindrical rod feels no torque due to a uniform flow, so the forcing will only enter the bend equation.

We proceed by performing a simple force balance on an infinitesimal segment of the filament. We resolve forces in the $x - z$ plane and $y - z$ plane separately, but notice that they are exactly the same. Figure 2.2 shows the force balance on a short piece of filament, making an angle of ϕ with the z -axis in the $x - z$ plane.

The forces here are as follows:

$$Q = -\frac{\delta E}{\delta X} = \text{elastic force} \quad (2.47)$$

$$R = U\zeta_{\parallel} \cos \phi = \text{parallel fluid drag} \quad (2.48)$$

$$T = \text{filament tension} \quad (2.49)$$

$$S = U\zeta_{\perp} \sin \phi + \zeta_{\perp} \frac{\partial X}{\partial t} \cos \phi = \text{normal drag due to flow and motion} \quad (2.50)$$

We resolve forces in the S direction:

$$S = Q \cos \phi \quad (2.51)$$

$$U\zeta_{\perp} \sin \phi + \zeta_{\perp} \frac{\partial X}{\partial t} \cos \phi = -\frac{\delta E}{\delta X} \cos \phi \quad (2.52)$$

$$\zeta_{\perp} \left(\frac{\partial X}{\partial t} + U \frac{\partial X}{\partial z} \right) = -\frac{\delta E}{\delta X} \quad (2.53)$$

where we use the fact that $\tan \phi = \frac{\partial X}{\partial z}$. We have made the assumptions that the filament is inextensible and is not moving along its longitudinal axis. This is equivalent

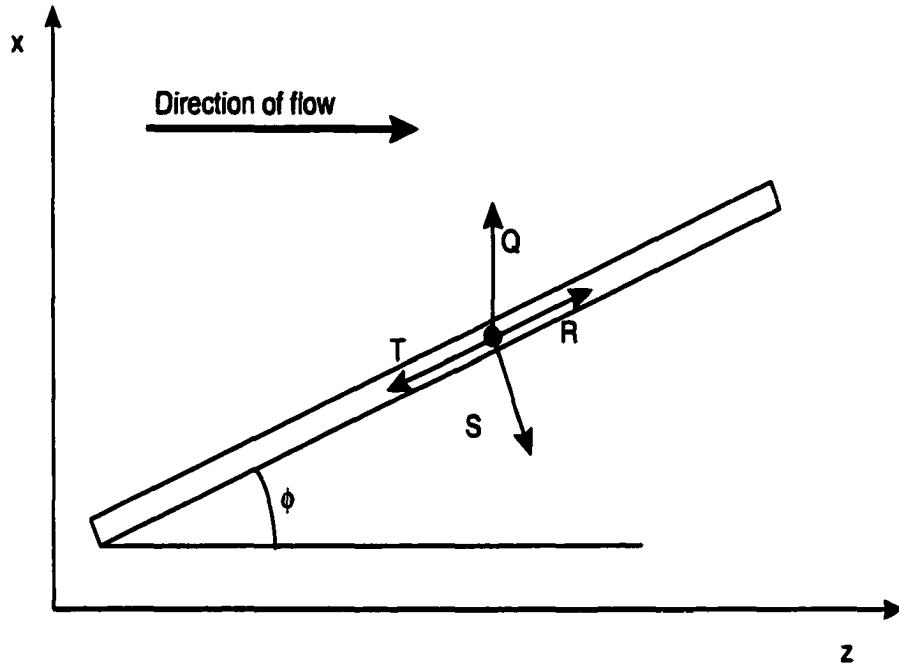


FIGURE 2.4. Force balance

to defining the force as above and setting the tension, $T = U\zeta_{\parallel} \cos \phi - \frac{\delta E}{\delta X} \sin \phi$ at all times and places.

By performing the analogous procedure in the $y - z$ plane, we thus replace 2.44, the dynamic equation of bending, with

$$\zeta_{\perp} \xi_t = -A(\xi_{zz} - \Omega_2^0 e^{i\theta})_{zz} - \zeta_{\perp} U \xi_z. \quad (2.54)$$

This establishes the basic partial differential equations which we will use in studying Hotani's experiments.

We can compare these to the equations found in [23]. Essentially, we are neglecting terms that scale as $O(\xi_z^2)$ (equation 2.12) and are not constraining the filament to have a strictly fixed length (rather, we are limiting the range of z values from 0 to L). We can estimate the magnitude of ξ_z by considering the relaxed state of the filament, a helix of radius $\Omega_2^0 P^2 / (2\pi)^2$ and pitch P . Taking Ω_2^0 and P as given in section 2.4, $\xi_z^2 \simeq .04$. Notice also the absence of a *writhe-tracking* piece in the twist

equation. This term, which would be present had we not linearised, includes the twisting response to bending motions out of the plane of the local curvature. It is shown in [38] that an inextensible, crankshaft-like rotating filament held fixed at the origin and aligned along the z -axis loses twist at a rate proportional to $1 - \hat{\mathbf{z}} \cdot \hat{\mathbf{t}}(L)$, that is, depending only on the local tangent vector at the free end. This term is rewritten as $(1 - \sqrt{1 - \xi_z(L)^2}) = \xi_z(L)^2 + O(\xi_z^4)$, so it seems we are consistent in omitting the writhe-tracking term. The question remains of whether any $O(\xi_z^2)$ terms are important to the qualitative study of Hotani's experiment.

2.3. Rescaling and dimensional analysis

Equations (2.54) and (2.45) are dimensional. We list the variables and parameters with dimensions in the following table.

Quantity	Physical interpretation	Dimension
ξ	Transverse displacement	L
θ	Rotation angle	1
A	Bend modulus	ML^3T^{-2}
ζ_{\perp}	Normal drag coefficient	$ML^{-1}T^{-1}$
Ω_2^0	Intrinsic curvature	L^{-1}
ζ_R	Rotational drag coefficient	MLT^{-1}
γ^2	Twist gradient energy scale	ML^5T^{-2}
U	Forcing flow speed	LT^{-1}
L	Filament length	L

TABLE 2.2. Model Parameters

The twist rate energy function $V(\theta_z)$ also contains physical information. Let us assume that the potential has minima at $\theta_z = \pm \frac{2\pi}{P}$ which are of similar depths and that the overall scale of the energy barrier is given by the dimensional parameter H , so

$$V(\theta_z) = H f\left(\frac{P\theta_z}{2\pi}\right). \quad (2.55)$$

Note the argument of f is non-dimensional.

One quite practical energy might be

$$V(\theta_z) = H \left(-\frac{1}{2} \left(\frac{P\theta_z}{2\pi} \right)^2 + \frac{1}{4} \left(\frac{P\theta_z}{2\pi} \right)^4 \right) \quad (2.56)$$

which is symmetric.

There are many energy, length and time scales to consider. Rather than laboriously computing each possible combination of the constants and cataloguing the possible scales, let us examine the physical situation.

The characteristic amplitude of the transverse (X - Y) displacement of the filament must be the natural length on which to scale ξ . As calculated above (2.39) this length will be the radius of the helix in a relaxed state, $\Omega_2^0(P/(2\pi))^2$.

In the z -direction, there are at least three possible length scales: L , the length of the whole filament, P , the pitch of a relaxed helix and finally the twist front width which we will call λ . Examining Hotani's micrographs, it is clear that λ is very short compared to the filament or pitch length. Physically, λ results from a balance of the twist gradient torque with the torque due to a helix hand reversal, in other words, a balance taking the form of $\gamma^2\theta_{zzzz} \sim \theta_{zz}V''(\theta_z)$. Dimensionally, then, $\gamma^2/\lambda^4 \sim (HP^2)/(2\pi\lambda)^2$ implying $\lambda \sim 2\pi\gamma/(P\sqrt{H})$. This makes sense: if γ^2 is big compared to H , then the system opposes sharp fronts, so λ represents a longer transition zone from one front to the next.

The choice of time scale is interesting. Any of the characteristic lengths, when divided by the forcing flow velocity U give a time scale characteristic of the flow. Physically, though, U is the control parameter the experimentalist (or numerical simulator) can adjust to change the behaviour of the flagellum. Thus we choose to look at the elastic dynamics to find an appropriate time scale. The elasto-hydrodynamic bend relaxation time $\zeta_{\perp}L^4/A$ is a candidate, where L could be any of the lengths described above. The twist equation gives two possible time scales for each length scale, depending on whether we balance elastic relaxation with the twist front piece,

$\zeta_R \theta_t \sim -\gamma^2 \theta_{zzzz}$ giving the time scale $T \sim L^4 \zeta_R / \gamma^2$ or with the twist potential, $\zeta_R \theta_t \sim \theta_{zz} V''(\theta_z)$ so $T \sim (2\pi L)^2 \zeta_R / (HP^2)$ (where L is any length scale).

Among the many choices of rescalings, we will focus on two. First, rescaling both length and time on the twist front scale to examine the front closely. We will call this the “inner” rescaling. Secondly, we will rescale on the pitch length and twist potential time scale which is more appropriate for study of the whole system (the “outer” rescaling).

We first perform the the inner rescaling, on the following scales:

$$z \rightarrow \lambda \alpha, t \rightarrow T \tau, \xi \rightarrow D \hat{\xi} \quad (2.57)$$

The scales chosen are: $\lambda = 2\pi\gamma / (P\sqrt{H})$ (this is the front width length scale, as above) and $T = \lambda^4 \zeta_R / \gamma^2$. We defer choice of D as it is unclear what the characteristic scale of ξ will be in this inner rescaling.

Equations (2.45) and (2.54) become

$$\hat{\xi}_\tau + u \hat{\xi}_\alpha = -\beta (\hat{\xi}_{\alpha\alpha} - \frac{\Omega_2^0 \gamma^2 (2\pi)^2}{DHP^2} e^{i\theta})_{\alpha\alpha} \quad (2.58)$$

$$\theta_\tau = -\theta_{\alpha\alpha\alpha\alpha} + \theta_{\alpha\alpha} f'' \left(\frac{P\theta_\alpha}{2\pi\lambda} \right) - D \frac{A\Omega_2^0 (2\pi)^2}{HP^2} \text{Im}(e^{i\theta} \hat{\xi}_{\alpha\alpha}^*) \quad (2.59)$$

The most natural choice is to take $D \rightarrow (\Omega_2^0 \gamma^2 (2\pi)^2) / (DHP^2)$ which is a rescaling of the intrinsic bend by λ^2 , and simplifies (2.58). We are left with

$$\hat{\xi}_\tau + u \hat{\xi}_\alpha = -\beta (\hat{\xi}_{\alpha\alpha} - e^{i\theta})_{\alpha\alpha} \quad (2.60)$$

$$\theta_\tau = -\theta_{\alpha\alpha\alpha\alpha} + \theta_{\alpha\alpha} f''(\theta_z / \eta) - \mu \text{Im}(e^{i\theta} \hat{\xi}_{\alpha\alpha}^*) \quad (2.61)$$

The dimensionless constants are

$$u = \frac{U\gamma\zeta_R}{H^{3/2}} \left(\frac{2\pi}{P} \right)^3 = \frac{\zeta_R \lambda^3}{\gamma^2} U \quad (2.62)$$

$$\beta = \frac{A\zeta_R}{\gamma^2 \zeta_\perp} \quad (2.63)$$

$$\mu = A \left(\frac{\Omega_2^0 \gamma}{H} \right)^2 \left(\frac{2\pi}{P} \right)^4 \quad (2.64)$$

$$\eta = \frac{H^{1/2}}{\gamma} \left(\frac{P}{2\pi} \right)^2 = \frac{1}{\lambda} \left(\frac{P}{2\pi} \right) \quad (2.65)$$

which are the rescaled velocity, bend modulus, coupling coefficient and potential scale respectively. As we would expect in this rescaling, the fourth-order piece of (2.61) balances the time derivative exactly. The dimensionless constants strongly depend on the pitch scale. This motivates our rescaling on the pitch length (the outer rescaling), to follow. Notice the balance between the bend elasticity scale (measured by A/ζ_{\perp}) and the twist-front piece (measured by γ^2/ζ_R) in β , which gives the rate of relaxation of $\hat{\xi}$ to the preferred state $e^{i\theta}$. A balance between A and H shows up in the coupling coefficient μ - the twist state of a flagellum is more influenced by the bend state if the bending rigidity exceeds the twisting rigidity.

The inner rescaling is particularly useful for studying the twist dynamics of the filament. However, in terms of the inner length λ , the filament has length at least 100. It will therefore be more practical to rescale on the length of the phenomena we are really interested in, the regions of chirality inversion. This means we should rescale on the pitch length, to obtain the outer rescaling:

Let $z = P\alpha$, and choose the time scale to match the twist potential, so $t = \tau((2\pi)^2\zeta_R)/H$. ξ is rescaled by a factor of $P^2\Omega_2^0$ - just the intrinsic bend rescaled using the pitch length. The equations of motion become

$$\hat{\xi}_{\tau} + u\hat{\xi}_{\alpha} = -c_b(\hat{\xi}_{\alpha\alpha} - e^{i\theta})_{\alpha\alpha} \quad (2.66)$$

$$\theta_{\tau} = -c_4\theta_{\alpha\alpha\alpha\alpha} + \theta_{\alpha\alpha}f''\left(\frac{\theta_{\alpha}}{2\pi}\right) - c_c\text{Im}(e^{i\theta}\hat{\xi}_{\alpha\alpha}^*) \quad (2.67)$$

with dimensionless constants

$$c_b = \frac{A(2\pi)^4\zeta_R}{\zeta_{\perp}HP^4} \quad (2.68)$$

$$u = \frac{(2\pi)^2\zeta_R U}{H} \quad (2.69)$$

$$c_4 = \frac{\gamma^2(2\pi)^2}{P^4H} \quad (2.70)$$

$$c_c = \frac{A(2\pi\Omega_2^0)^2}{H}. \quad (2.71)$$

In this rescaling, we see that the preferred twist states correspond to $\Omega = \theta_{\alpha} = 2\pi$.

We shall use this rescaling in the numerical solution of the equation (discussed in chapter 4).

We can perform a very interesting scaling analysis to determine how the velocity of a propagating helix-hand reversal will scale with the applied fluid flow speed.

First note that the torque T on a helix of radius R , pitch P and length L caused by a flow of speed U is [39]

$$T = \frac{2\pi UR^2 L \zeta_{\parallel}}{(P^2 + 4\pi^2 R^2)^{1/2}} \quad (2.72)$$

where ζ_{\parallel} is the drag coefficient per unit length for motions parallel to the filament, equal to $\zeta_{\perp}/2$. We shall call the flow velocity just sufficient to cause a perversion to be nucleated at the attached end U^* , and the initial velocity of this front \mathcal{U} . We now argue that, to first order, the power of this propagating front must scale like

$$T\mathcal{U}\Delta\Omega, \quad (2.73)$$

where $\Delta\Omega = 2\left(\frac{2\pi}{P}\right)$ is the difference in twist rates between the two stable states (where we assume that the pitches of the left- and right-handed states are the same for simplicity). Additionally, the work done by this invading front (per second) will scale like $\zeta_{\perp}L(\omega R)^2$ where ω is the angular speed of rotation of the filament downstream from the perversion. Geometrically, ω must be equal to the front speed \mathcal{U} times the equilibrium twist rate $\frac{2\pi}{P}$. Balancing these two powers at the critical flow rate U^* , and assuming that R is the same for both the original and invading helix, we have

$$\frac{\pi U^* R^2 L \zeta_{\perp} \mathcal{U} \Delta\Omega}{(P^2 + 4\pi^2 R^2)^{1/2}} = \zeta_{\perp} L \left(\mathcal{U} \frac{2\pi}{P} R \right)^2 \quad (2.74)$$

which simplifies to

$$\mathcal{U} \simeq \frac{U^* P}{(P^2 + 4\pi^2 R^2)^{1/2}} \quad (2.75)$$

This scaling shows that, at the critical torque necessary to nucleate a perversion at the fixed end, the speed of the initial invasion of the front depends only on the geometry

of the helix and the flow rate. The radius and pitch of real flagella are in fact of the same order of magnitude, and so this relation simplifies further to $U \simeq 0.3U^*$. Note that this result only applies to the invasion of the first polymorphic front into a filament of one handedness. We will compare our numerical results to this scaling result in section 4.2.

2.4. Physical parameters

We summarise the problem parameters and estimates in the following table.

Quantity	Approximate Value	Unit
L	10-15	μm
P	1	μm
Ω_2^0	12000	cm^{-1}
ζ_{\perp}	1	$\text{g}/(\text{cm s})$
ζ_R	10^{-13}	g cm/s
A	10^{-15}	erg cm
γ	10^{-13}	$(\text{erg cm}^3)^{1/2}$
U	10	$\mu\text{m/s}$
H	10^{-6}	erg/cm

TABLE 2.3. Parameter values

The parameters L , P and Ω_2^0 are easily estimated from Hotani's measurements. To find the drag coefficients we need to use formulae (2.23) and (2.24), which require the diameter of the filament (23nm) and the viscosity of the fluid. Hotani's experimental fluid was a methylcellulose solution with viscosity of 50-100 centipoise.

Experimental determinations of the elastic properties of flagella are few. An interesting study of torsional rigidity is that of Block, Blair and Berg, [40] in which bacteria tethered to a glass surface by one of their flagella are held using an optical trap [41]. The trap is then moved in a circle around the tether point. The bacteria were treated to make their motors inactive, and certain cells were found to have motors that appeared to be "locked" in that the flagellum was unable to rotate relative

to the cell body. The strength of the rotating trap was varied. At each strength, the cell would rotate until the torque due to the trap was equal to the elastic reaction of the tethering flagellum. The rotation angle was measured and a plot of this angle against applied torque produced. For small torques, the reaction was approximately linear with constant $k_\theta = 4 \times 10^{-12}$ dyne-cm/rad. Using the formula for the torsional rigidity μ [29], $k_\theta = \pi\mu(R^4 - r^4)/2L$ for a tube of inner and outer radii r and R respectively, and length L , one calculates ($R = 7\text{nm}$, $r = 3\text{nm}$, $L = 0.2\mu\text{m}$ here) $\mu \simeq 2 \times 10^8$ dyne/cm². This result is for *Salmonella* type bacteria. The corresponding torsional rigidity for *E. Coli* is estimated to be at least 5×10^9 dyne/cm². A later paper [42] revealed that this rigidity was essentially that of the hook part of the flagellum. What was actually happening was that the hook was winding up at low torques while the flagellar filament, which is more rigid, was not. This result is thus crucial for studying the entire flagellar assembly. We, however, are interested in Hotani's experiment in which there is just the filament section so the hook is not important.

An earlier pair of papers [43] estimate the modulus of rigidity and the Young modulus, E by examining the elongation of a helical filament (no attached hook) attached to a slide at one end with a fluid flow, exactly as in the Hotani experiment. They estimated the elastic energy of a filament essentially as an integral of the form of (2.29), and calculated the torque on the helix due to the unwinding drag of the flow. Together these two calculations gave an estimate that $\mu \simeq 10^{11}$ or 10^{12} dyne/cm². μ is related to the parameter C in (2.29) by $C = \mu\pi R^4/2$. In the bistable potential we wish to consider, the curvature of each potential well should be governed by this scale.

In fact, throughout this work we shall make the considerable simplification of using a simple symmetric quartic potential with wells of equal depth corresponding to opposing helices of equal pitch. The only remaining parameter will be the height of the separating barrier. We are principally concerned with proving that this is an appropriate approximate model for the system under consideration, rather than with

attempting to reproduce nature in every detail. In making this approximation, we are overlooking the different pitches of the normal and semi-coiled states observed in experiment, and we will not be able to control the curvature of the potential in the wells to be that discovered above (although to do so would not be difficult).

In estimating H , the barrier height, we use Hotani's calculation of the torque required to initiate a transition from the normal to semi-coiled state, $T = 10^{-12}$ dyne cm. The simplest estimate we can make [44] is that $H \simeq \frac{2\pi T}{P}$ where P is a preferred pitch. We find from this that $H \simeq 10^{-7}$ erg/cm.

The bending modulus A was measured by Fujime et al [45] in a complicated experiment based on measuring the scattering of light passing through a flagellar solution. Broadly speaking, the thermal fluctuations of the flagella in solution were picked up as a term in the width of the scattering peak corresponding to the spatial frequency of flagella in the solution. If this term was large, each flagella was undergoing considerable distortion due to thermal noise, and so the bend modulus must have been small, and vice versa. The calculated value in the paper was $A \simeq 10^{-15}$ dyne cm², however the flagellar radius used in the calculations was incorrect - the value is recalculated in [43] with the correct value and is a little larger, $A \simeq 5 \times 10^{-15}$ dyne cm².

Finally we compute γ , the parameter controlling the width of the interface between domains of different chirality. We can calculate the steady, unforced front solution of (2.45), $H f'(\frac{P\theta_z}{2\pi}) = \gamma^2 \theta_{zzz}$ for an infinitely long filament which, for the simple symmetric potential given by (2.56) turns out to be $\theta_z = \frac{2\pi}{P} \tanh(\frac{z}{l})$ where the length scale of the front is set by $l = \sqrt{(H\pi)/(P\gamma^2)}$. The front width computed from Hotani's micrographs is on the order of 50nm-.2 μ m [23], so equating $l = .1\mu$ m we will use $\gamma^2 \sim 100\pi H/P$ to obtain the correct front width.

3. PERTURBATION ANALYSES

In this chapter we study two simplified systems related to the bend and twist equations derived for a bistable helical rod. Firstly we look at the twist equation in the absence of any bending forces and determine whether, in the case that the potential f is asymmetric, a travelling front linking regions of the rod carrying different twist states will occur. We then examine how a singly stable helical rod (which has a single preferred handedness) is unwound by slow flow along its axis.

3.1. Bistable twisted rod

We begin by examining the simple case of a twisted but unbent rod of length $2L$ with a bistable twist energy. Using the inner rescaling, such a rod will have twist equation

$$\theta_\tau = -\theta_{\alpha\alpha\alpha\alpha} + \theta_{\alpha\alpha} f''(\theta_{\alpha\alpha}/\eta) \quad (3.1)$$

from (2.61) ($\alpha = z/\lambda$). We make one additional simplifying modification and rescale θ to absorb the pitch factor, and obtain

$$\theta_\tau = -\theta_{\alpha\alpha\alpha\alpha} + \theta_{\alpha\alpha} f''(\theta_{\alpha\alpha}). \quad (3.2)$$

Rescaled Ω - dynamics are found by differentiating once with respect to α (in this case, arc length s and straight line distance z are the same):

$$\Omega_\tau = -\partial_{\alpha\alpha} (\Omega_{\alpha\alpha} - V'(\Omega)). \quad (3.3)$$

The energy of such a rod may be written compactly as

$$E[\Omega] = \int_{-L}^L \left(f(\Omega) + \frac{1}{2} \Omega_\alpha^2 \right) d\alpha. \quad (3.4)$$

We will choose $f(\Omega) = -\frac{1}{2}\Omega^2 + \frac{1}{4}\Omega^4$. The stable values are therefore $\Omega = \pm 1$, separated by a barrier of height $\frac{1}{4}$. This choice gives a convenient stationary front solution (neglecting the boundary conditions) of (3.3)

$$\Omega^0 = \tanh\left(\alpha/\sqrt{2}\right). \quad (3.5)$$

We now ask a natural question, namely, if we modify the potential f so that one well is deeper than the other, will the more stable configuration invade the other? We would expect the solution to be close to Ω^0 in shape but be translating.

The answer to the question will depend on the boundary conditions we impose. The most natural boundary conditions for a free filament (arising from the functional differentiation of (3.4) and corresponding to stress free ends) are $(f'(\Omega) - \Omega_{\alpha\alpha}) = 0$ and $\Omega_{\alpha} = 0$ at both ends. In the infinite case where $\lim_{\alpha \rightarrow \pm\infty} \Omega = \pm 1$ we then have that $(f'(\Omega) - \Omega_{\alpha\alpha})_{\alpha} = 0$ at infinity. Integrating (3.3), we obtain

$$\frac{\partial}{\partial t} \int_{-L}^L \Omega d\alpha = -[(\Omega_{\alpha\alpha} - f'(\Omega))_{\alpha}]_{-L}^L. \quad (3.6)$$

In the event that $L = \infty$ we have a conservation law for Ω , and there is no simple travelling front solution of (3.3). However, the situation is not so simple for a filament of finite length. Ω^0 (3.5) is not a stationary solution of (3.3) with the natural boundary conditions and symmetric potential f , for its derivative does not vanish in a finite length region. Assuming that L is large, though, the stationary front solution should differ from Ω^0 by only a small perturbation (this statement could be verified by an argument that essentially the solution of the boundary value problem will be continuous in the parameter L).

We will look at the case where f is slightly asymmetric by replacing it with $f + \epsilon W$. Let $W(\Omega) = \frac{1}{3}\Omega^3 - \Omega$ so that $f(\Omega) + \epsilon W(\Omega)$ has minima at $\Omega = \pm 1$ with difference in energy equal to $\frac{-4\epsilon}{3}$, separated by a maximum at $(-\epsilon, \frac{-1}{12}\epsilon^2(\epsilon^2 - 6))$. All perturbation expansions will be made in the small parameter ϵ .

We look for a travelling solution of the form $\Omega(\sigma)$ where $\sigma = \alpha - c\tau$ is the travelling wave coordinate with speed c . As we are working in a finite domain, the front speed

obtained by this method will only be valid for times small compared to L/c . The travelling wave reduction of(3.3) is then

$$-c\Omega_\sigma = -\partial_{\sigma\sigma} (\Omega_{\sigma\sigma} - (f + \epsilon W)'(\Omega)). \quad (3.7)$$

We shall use the following boundary conditions at $z = \pm L$:

$$(\Omega_{\alpha\alpha} - f'(\Omega)) = 0 \quad (3.8)$$

$$\partial_\alpha(\Omega_{\alpha\alpha} - f'(\Omega)) = 0 \quad (3.9)$$

For large L these are extremely close to the natural boundary conditions, with the significant benefit that they admit Ω^0 as a stationary solution of the unperturbed problem.

We perturb about the stationary solution: $\Omega = \Omega^0 + \epsilon\Omega^1 + \dots$. The perturbed boundary conditions (obtained by substituting $\Omega^0 + \epsilon\Omega^1$ and $f + \epsilon W$ in the original boundary conditions) are at order 0

$$(\Omega_{\alpha\alpha}^0 - f(\Omega)) = 0 \quad (3.10)$$

$$(\Omega_{\alpha\alpha}^0 - f(\Omega))_\alpha = 0 \quad (3.11)$$

$$(3.12)$$

and at order ϵ :

$$\partial_\alpha(f''(\Omega^0)\Omega^1 + W'(\Omega_0) - \Omega_{\alpha\alpha}^1) = 0 \quad (3.13)$$

$$(f''(\Omega^0)\Omega^1 + W'(\Omega_0) - \Omega_{\alpha\alpha}^1)_\alpha = 0 \quad (3.14)$$

The front speed c is also expanded as $c = 0 + \epsilon c_1 + \dots$. Expanding in ϵ then gives at order 1:

$$0 = \partial_{\sigma\sigma}(f'(\Omega^0) - \Omega_{\sigma\sigma}^0) \quad (3.15)$$

as it should be. At $O(\epsilon)$:

$$-c_1\Omega_\sigma^0 = \partial_{\sigma\sigma}(f''(\Omega^0)\Omega^1 + W'(\Omega^0) - \Omega_{\sigma\sigma}^1) \quad (3.16)$$

which is rewritten as

$$L[\Omega^1] = -c_1 \Omega_\sigma^0 - \partial_{\sigma\sigma}(W'(\Omega^0)) \quad (3.17)$$

where the linear operator L is defined by

$$L[\Omega^1] = \partial_{\sigma\sigma}(f''(\Omega^0)\Omega^1 - \Omega_{\sigma\sigma}^1). \quad (3.18)$$

Our procedure will now be a standard Fredholm alternative argument [46] to find value(s) of c_1 which permit a solution of (3.17). First, we compute the adjoint operator to L . u is a test function satisfying the above boundary conditions for Ω^1 . The boundary conditions on v (the dual manifold) will be determined by making the boundary terms in the integration vanish.

$$\langle Lu, v \rangle = \int_{-L}^L \partial_{\sigma\sigma}(u f''(\Omega^0) - u_{\sigma\sigma}) v d\sigma \quad (3.19)$$

$$= B_1 - B_2 + B_3 - B_4 + \int_{-L}^L u(f''(\Omega^0)v_{\sigma\sigma} - v_{\sigma\sigma\sigma\sigma}) d\sigma \quad (3.20)$$

$$= \langle u, L^* v \rangle \quad (3.21)$$

$$B_1 = [v(u f''(\Omega^0) - u_{\sigma\sigma})_\sigma]_{-L}^L \quad (3.22)$$

$$B_2 = [v_\sigma(u f''(\Omega^0) - u_{\sigma\sigma})]_{-L}^L \quad (3.23)$$

$$B_3 = [v_{\sigma\sigma} u_\sigma]_{-L}^L \quad (3.24)$$

$$B_4 = [v_{\sigma\sigma\sigma} u]_{-L}^L \quad (3.25)$$

B_1 and B_2 are zero from the boundary conditions on u . $L^* = f''(\Omega^0)\partial_{\sigma\sigma} - \partial_{\sigma\sigma\sigma\sigma}$ therefore acts on the space of functions v which satisfy $v_{\sigma\sigma\sigma}(\pm L) = v_{\sigma\sigma}(\pm L) = 0$.

Functions in the null space of L^* have the form

$$v = C_1 + C_2 \sigma + C_3 f_1 + C_4 f_2 \quad (3.26)$$

$$f_1 = \log \cosh\left(\frac{\sigma}{\sqrt{2}}\right) \quad (3.27)$$

$$f_2 = C_4 \int^\sigma (\cosh(\sqrt{2}\sigma') + 3\sqrt{2}\sigma' \tanh(\frac{\sigma'}{\sqrt{2}})) d\sigma' \quad (3.28)$$

$$(3.29)$$

Obviously constant and linear functions are permitted by the boundary conditions on v . Although individually f_1 and f_2 fail to satisfy the boundary conditions, it's possible that a linear combination of them might. We therefore need to investigate whether there exists a constant λ such that $\lambda(f_1)_{\sigma\sigma} + (f_2)_{\sigma\sigma} = 0$ and $\lambda(f_1)_{\sigma\sigma\sigma} + (f_2)_{\sigma\sigma\sigma} = 0$ simultaneously. A quick calculation shows that no such λ exists, so the null space of L^* is spanned by constants and linear functions. We integrate each of these against the right hand side of (3.17), set to zero and solve for c_1 . Note: $W'(\Omega^0) = \tanh^2(\frac{\sigma}{\sqrt{2}}) - 1$. First, the constant piece:

$$\int_{-L}^L -c_1 \Omega_\sigma^0 - \partial_{\sigma\sigma}(W'(\Omega^0)) d\sigma = [-c_1 \Omega^0 - \partial_\sigma(W'(\Omega^0))]_{-L}^L = 0 \quad (3.30)$$

$$c_1 = -\sqrt{2} \operatorname{sech}^2(L/\sqrt{2}) \quad (3.31)$$

Integrating against the function σ ,

$$\int_{-L}^L -c_1 \Omega_\sigma^0 - \partial_{\sigma\sigma}(W'(\Omega^0)) d\sigma \quad (3.32)$$

we notice that Ω_σ^0 is even so the c_1 -part integrates to zero. $\partial_{\sigma\sigma}(W'(\Omega^0))$ is also even so the other part integrates to zero. So there's no condition on c_1 from the linear piece. To $O(\epsilon)$ we now have the initial front speed

$$c = -\frac{2}{1 + \cosh L} \epsilon. \quad (3.33)$$

As $L \rightarrow \infty$ the front speed goes to zero exponentially, matching the fact that $c \rightarrow 0$ at $L = \infty$.

Although the preceding calculation was interesting, it applies only to a free filament. Of more relevance to the Hotani experiment is the case of a filament held fixed at one end. To study this case we will need to return to $\theta = \int^\alpha \Omega d\alpha$. We write the elastic energy of the rod in terms of θ :

$$E = \int_{-L}^L (f(\theta_\alpha) - \theta_{\alpha\alpha}^2) d\alpha \quad (3.34)$$

with boundary conditions

$$\theta(-L) = 0 \quad (3.35)$$

$$\theta_{\alpha\alpha}(-L) = 0 \quad (3.36)$$

$$\theta_{\alpha\alpha}(L) = 0 \quad (3.37)$$

$$f'(\theta_\alpha(L)) - \theta_{\alpha\alpha\alpha}(L) = 0 \quad (3.38)$$

The dynamical equation is now

$$\theta_\tau = f''(\theta_\alpha)\theta_{\alpha\alpha} - \theta_{\alpha\alpha\alpha\alpha} = \partial_\alpha(f'(\theta_\alpha) - \theta_{\alpha\alpha\alpha}) \quad (3.39)$$

The function $\theta^0(\alpha) = \sqrt{2}(\log \cosh(\alpha/\sqrt{2}) - \log \cosh(L/\sqrt{2}))$ satisfies the equation and the fixed ($\alpha = 0$) boundary condition. It does not satisfy the other boundary conditions. But as L increases the error in the boundary conditions goes to zero exponentially. In fact, if $L = 50$ (meaning the filament has length 100 front widths, typical for a flagellum), $\theta_{\alpha\alpha}^0(\pm 100) \simeq 10^{-31}$ and $f'(\theta_\alpha^0(100)) - \theta_{\alpha\alpha\alpha}^0(100) \simeq 10^{-30}$ also.

It therefore seems reasonable to assume there is a steady state solution for reasonably long filaments which is a very small perturbation of θ^0 (again, to make this a rigorous statement we should make an argument that the solution should vary continuously in the parameter L). We look for uniformly translating solutions: ($\sigma = \alpha - c\tau$) and find

$$-c\theta_\sigma = f''(\theta_\sigma)\theta_{\sigma\sigma} - \theta_{\sigma\sigma\sigma\sigma} \quad (3.40)$$

We will defer the obvious integration until after the perturbation. The boundary conditions for this equation are taken to be simple rewritings of (3.35-3.38). The front speed we obtain is therefore (again) valid only for short times.

We now perturb: $f \rightarrow f + \epsilon W, \theta \rightarrow \theta^0 + \epsilon\theta^1$ and $c \rightarrow c^0 + \epsilon c^1$. At order 1:

$$-c^0\theta_\sigma^0 = f''(\theta_\sigma^0)\theta_{\sigma\sigma}^0 - \theta_{\sigma\sigma\sigma\sigma}^0 \quad (3.41)$$

so $c^0 = 0$, as expected. At order ϵ :

$$-c^1 \theta_\sigma^0 = f''(\theta_\sigma^0) \theta_{\sigma\sigma}^1 + f'''(\theta_\sigma^0) \theta_{\sigma\sigma}^0 \theta_\sigma^1 + W'''(\theta_\sigma^0) \theta_{\sigma\sigma}^0 - \theta_{\sigma\sigma\sigma\sigma}^1 \quad (3.42)$$

$$= (W'(\theta_\sigma^0) + f''(\theta_\sigma^0) \theta_\sigma^1 - \theta_{\sigma\sigma\sigma}^1)_\sigma \quad (3.43)$$

$$\theta_{\sigma\sigma}^1(-L) = 0 \quad (3.44)$$

$$\theta^1(\pm L) = 0 \quad (3.45)$$

$$f''(\theta_\sigma^0(L)) \theta_\sigma^1(L) = \theta_{\sigma\sigma\sigma}^1(L) \quad (3.46)$$

We rewrite this as

$$L[\theta^1] = N[\theta^0] \quad (3.47)$$

where

$$L[\theta^1] = f''(\theta_\sigma^0) \theta_{\sigma\sigma}^1 + f'''(\theta_\sigma^0) \theta_{\sigma\sigma}^0 \theta_\sigma^1 - \theta_{\sigma\sigma\sigma\sigma}^1 \quad (3.48)$$

$$= \frac{\partial}{\partial \sigma} (f''(\theta_\sigma^0) \theta_\sigma^1 - \theta_{\sigma\sigma\sigma}^1) \quad (3.49)$$

The procedure is now the same (Fredholm alternative argument) as above to fix c^1 . First we must find L^* by integrating by parts four times. All integrals are over the interval $[-L, L]$.

$$\langle Lu, v \rangle = \int \frac{\partial}{\partial \sigma} (f''(\theta_\sigma^0) u_\sigma - u_{\sigma\sigma\sigma}) v d\sigma \quad (3.50)$$

$$= B_1 - B_2 + B_3 - B_4 + \int u (f'''(\theta_\sigma^0) \theta_{\sigma\sigma}^0 v_\sigma + f''(\theta_\sigma^0) v_{\sigma\sigma} - v_{\sigma\sigma\sigma\sigma}) d\sigma$$

$$B_1 = [(f''(\theta_\sigma^0) u_\sigma - u_{\sigma\sigma\sigma}) v]_{-L}^L \quad (3.51)$$

$$B_2 = [(f''(\theta_\sigma^0) v_\sigma u - u_{\sigma\sigma}) v_\sigma]_{-L}^L \quad (3.52)$$

$$B_3 = [-v_{\sigma\sigma} u_\sigma]_{-L}^L \quad (3.53)$$

$$B_4 = [-v_{\sigma\sigma\sigma} u]_{-L}^L \quad (3.54)$$

Applying the boundary conditions on u and requiring that the B_i vanish we obtain

the following conditions on v :

$$v(-L) = 0 \quad (3.55)$$

$$v_{\sigma\sigma}(\pm L) = 0 \quad (3.56)$$

$$f''(\theta_\sigma^0(L))v_\sigma(L) = v_{\sigma\sigma\sigma}(L) \quad (3.57)$$

We need to find the solutions of

$$L^*[v] = \theta_{\sigma\sigma}^0 f'''(\theta_\sigma^0)v_\sigma + f''(\theta_\sigma^0)v_{\sigma\sigma} - v_{\sigma\sigma\sigma\sigma} = 0 \quad (3.58)$$

We immediately see $v = \text{constant}$ is a solution. Letting $w = v_\sigma$ and integrating once we obtain $f''(\theta_\sigma^0)w - w_{\sigma\sigma} = \text{constant} = 0$. This has solutions $w_1 = \text{sech}^2(\sigma/2)$ and $w_2 = \text{sech}^2(\sigma/2)(12\sigma + 8\sqrt{2}\sinh(\sqrt{2}\sigma) + \sqrt{2}\sinh(2\sqrt{2}\sigma))$. Applying reduction of order to the original equation yields the fourth solution, written below. The null space of L^* is spanned by linear combinations of the following functions which satisfy the boundary conditions.

$$v_1 = C_1 \quad (3.59)$$

$$v_2 = C_2 \tanh(\sigma/\sqrt{2}) \quad (3.60)$$

$$v_3 = C_3 \int^\sigma w_2(\sigma') d\sigma' \quad (3.61)$$

$$v_4 = C_4 \frac{(12\sigma + 8\sqrt{2}\sinh(\sqrt{2}\sigma) + \sqrt{2}\sinh(2\sqrt{2}\sigma)) \tanh(\sigma/\sqrt{2})}{6\sqrt{2}\sigma + 8\sinh(\sqrt{2}\sigma) + \sinh(2\sqrt{2}\sigma)} \quad (3.62)$$

We find there is no non-trivial v satisfying the boundary conditions. However, as $L \rightarrow \infty$, $v = \tanh(\sigma/2) + \tanh(L/2)$ becomes close to a solution. The true solution for finite L will presumably be a small perturbation of this, in the same way that a perturbation of θ^0 will solve the steady state problem above. The Fredholm condition on c^1 in the limit $L \rightarrow \infty$ is then

$$\int_{-L}^L \left(\tanh(\sigma/\sqrt{2}) + \tanh(L/\sqrt{2}) \right) (-c^1 \theta_\sigma^0 - W''(\theta_\sigma^0) \theta_{\sigma\sigma}^0) d\sigma = 0 \quad (3.63)$$

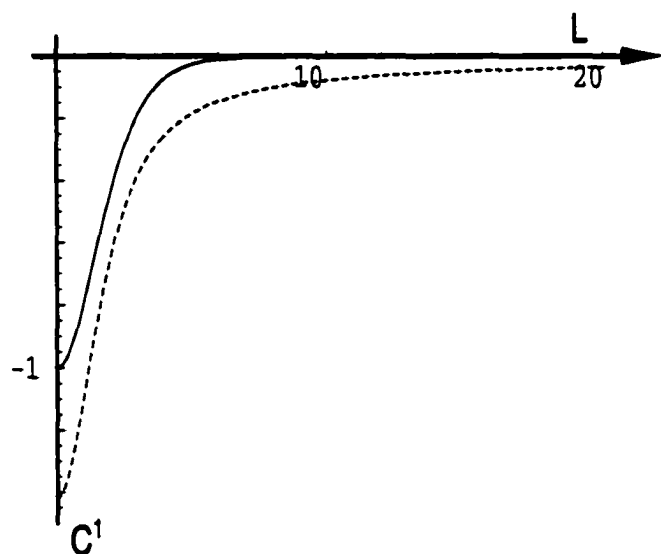


FIGURE 3.1. Comparison of front propagation speeds as functions of the filament half-length L for twisted rods with different boundary conditions. The solid line corresponds to the front speed where the filament is free at both ends (equation (3.33)). The dashed line corresponds to the front speed for a rod clamped at one end (equation (3.65)).

which turns out to be:

$$c^1 = \frac{2 \tanh^3(L/\sqrt{2})}{3(\sqrt{2} \tanh(L/\sqrt{2}) - L)} \quad (3.64)$$

For large L this is asymptotically

$$c \sim \frac{2}{3(\sqrt{2} - L)} \epsilon \quad (3.65)$$

We can compare this front speed (with a clamped end) to that obtained using two free ends above (3.33). The front speed in the free - free case decayed as e^{-L} whereas here it decays as $1/L$, which is considerably slower. See figure 3.1.

3.2. Singly stable driven helical rod

We now move to a case closer to the Hotani experiment, that of a **single-handed** helix, one which has a single preferred handedness of pitch P in dimensionless length

units. So $V(\Omega) = \frac{1}{2}(\Omega - R)^2$, for example, where $R = 2\pi/P$. The governing equations (using the inner rescaling) are (2.60,2.61)

$$\xi_t = \beta(e^{i\theta} - \xi_{\alpha\alpha})_{\alpha\alpha} - U\xi_{\alpha} \quad (3.66)$$

$$\theta_t = -\nu \text{Im}(e^{i\theta} \xi_{\alpha\alpha}^*) - \theta_{\alpha\alpha\alpha\alpha} + \theta_{\alpha\alpha} \quad (3.67)$$

with eight all-important boundary conditions

$$\xi(0) = 0 \quad (3.68)$$

$$\xi_{\alpha\alpha}(0) = 1 \quad (3.69)$$

$$\xi_{\alpha\alpha}(L) = e^{i\theta(L)} \quad (3.70)$$

$$\xi_{\alpha\alpha\alpha}(L) = i\theta_{\alpha}(L)e^{i\theta(L)} \quad (3.71)$$

$$\theta(0) = 0 \quad (3.72)$$

$$\theta_{\alpha\alpha}(0) = 0 \quad (3.73)$$

$$\theta_{\alpha\alpha}(L) = 0 \quad (3.74)$$

$$\theta_{\alpha\alpha\alpha}(L) = V'(\theta_{\alpha}(L)) = \theta_{\alpha}(L) - R \quad (3.75)$$

The important fact here is in equation (3.67) - the second derivative of the twist potential, multiplying $\theta_{\alpha\alpha}$, is now just 1. This is a considerable simplification over the bistable potential case.

In the case of no applied flow, the above equations (3.66), (3.67) reduce to the following:

$$0 = (e^{i\theta} - \xi_{\alpha\alpha})_{\alpha\alpha} \quad (3.76)$$

$$0 = -\nu \text{Im}(e^{i\theta} \xi_{\alpha\alpha}^*) - \theta_{\alpha\alpha\alpha\alpha} + \theta_{\alpha\alpha} \quad (3.77)$$

Integrate the bend equation twice and use the boundary conditions to get $\xi_{\alpha\alpha} = e^{i\theta}$. Then, substituting into the θ equation, we must solve $\theta_{\alpha\alpha\alpha\alpha} = \theta_{\alpha\alpha}$ subject to the above boundary conditions. The solution turns out to be $\theta = R\alpha$, essentially selected by the boundary condition (3.75). This is exactly what we would expect - the twist

rate sits at the bottom of the potential and the bend is such that the shape is an exact helix. Now we integrate $\xi_{\alpha\alpha}$ twice and apply the boundary conditions, to obtain

$$\xi = \frac{1}{R^2}(1 - e^{iR\alpha}) + K\alpha \quad (3.78)$$

where K is an undetermined constant. This corresponds to the overall angle the helix makes with the α axis. The approximation we made in deriving equation (3.66) requires that ξ_α is as small as possible. It is therefore best to take $K = 0$. When the flow is turned on we can justify this by saying that the helix will tend to line up as best it can with the flow (which is along the α axis). In the computer simulations K is chosen so that the average value of ξ is zero.

We will now switch on the applied flow U and ask how the twist and bend configurations of the filament will respond, in the steady state. The bend equation is

$$0 = (e^{i\theta} - \xi_{\alpha\alpha})_{\alpha\alpha} - \lambda\xi_\alpha \quad (3.79)$$

where $\lambda = U/\beta$ is assumed to be small. We will expand ξ and θ in powers of this small parameter about the $U = 0$ solution obtained above (3.78).

$$\theta = R\alpha + \lambda\hat{\theta} \quad (3.80)$$

$$\xi = \frac{1}{R^2}(1 - e^{iR\alpha}) + \lambda\hat{\xi} \quad (3.81)$$

First, expand the bend equation. At $O(\lambda)$:

$$0 = (e^{iR\alpha}i\hat{\theta} - \hat{\xi}_{\alpha\alpha})_{\alpha\alpha} + i\frac{e^{iR\alpha}}{R} \quad (3.82)$$

Now the twist equation:

$$0 = -\nu\text{Im}(\hat{\theta}i + \hat{\xi}_{\alpha\alpha}^* e^{iR\alpha}) - \hat{\theta}_{\alpha\alpha\alpha} + \hat{\theta}_{\alpha\alpha} \quad (3.83)$$

It is important to work with the correct perturbed boundary conditions:

$$\hat{\xi}(0) = 0 \quad (3.84)$$

$$\hat{\xi}_{\alpha\alpha}(0) = 0 \quad (3.85)$$

$$\hat{\xi}_{\alpha\alpha}(L) = ie^{iRL}\hat{\theta}(L) \quad (3.86)$$

$$\hat{\xi}_{\alpha\alpha\alpha}(L) = e^{iRL}(i\hat{\theta}_{\alpha}(L) - R\hat{\theta}(L)) \quad (3.87)$$

$$\hat{\theta}(0) = 0 \quad (3.88)$$

$$\hat{\theta}_{\alpha\alpha}(0) = 0 \quad (3.89)$$

$$\hat{\theta}_{\alpha\alpha}(L) = 0 \quad (3.90)$$

$$\hat{\theta}_{\alpha\alpha\alpha}(L) = \hat{\theta}_{\alpha}(L) \quad (3.91)$$

By integrating equation (3.82) twice and applying the boundary conditions we obtain

$$\hat{\xi}_{\alpha\alpha} = e^{iR\alpha}i\hat{\theta} + \frac{i}{R^3}(1 - e^{iR\alpha}) - i\alpha\frac{1 - e^{iRL}}{LR^3} \quad (3.92)$$

This may now be inserted into (3.83) and some unpleasant work performed to get the twist perturbation equation:

$$\hat{\theta}_{\alpha\alpha\alpha\alpha} - \hat{\theta}_{\alpha\alpha} = \frac{\nu}{R^3} \left(-1 + \frac{\alpha}{L} (\cos R(L - \alpha) - \cos R\alpha) \right) \quad (3.93)$$

The solution of this equation will be of the form

$$\hat{\theta}(\alpha) = C_1e^{\alpha} + C_2e^{-\alpha} + C_3 + C_4\alpha + P(\alpha) \quad (3.94)$$

where the C_i are constants and $P(\alpha)$ is a particular integral. We can explicitly compute P [47]:

$$P(\alpha) = \frac{\nu}{2R^3}\alpha^2 + \frac{\nu((L - \alpha)\cos R\alpha + \alpha\cos R(\alpha - L))}{LR^6} + \frac{2\nu(1 + 2R^2)}{LR^6(1 + R^2)^2}(\sin R\alpha - \sin R(\alpha - L)) \quad (3.95)$$

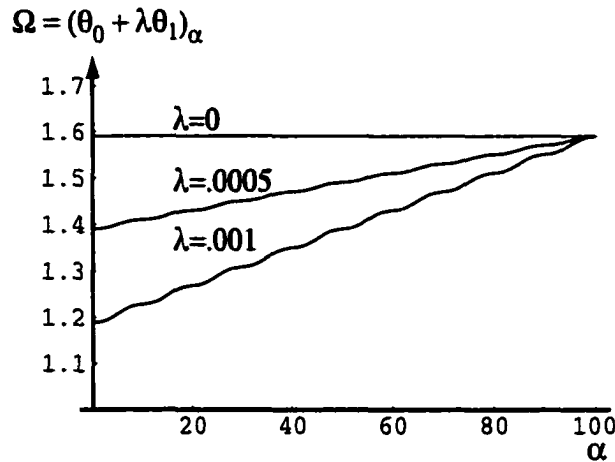


FIGURE 3.2. Singly stable helix twist rate under extensive flow.

together with the coefficients

$$C_1 = -\frac{L\nu R(1+R^2) + 2\nu \sin(LR)}{(1+e^L)LR^2(1+R^2)^2} \quad (3.96)$$

$$C_2 = -\frac{\nu e^L(LR(1+R^2) - 2\sin(LR))}{(1+e^L)LR^2(1+R^2)^2} \quad (3.97)$$

$$C_3 = \frac{\nu(R^2-1)}{R^5} - \frac{2\nu \sin LR}{LR^5} \quad (3.98)$$

$$C_4 = -\frac{\nu L}{R^3} - \frac{\nu(\cos LR - 1)}{LR^5} \quad (3.99)$$

Altogether this specifies the correction $\hat{\theta}$, but not in a particularly clear form. We plot as figure 3.2 the twist rate $(R\alpha + \lambda\hat{\theta}/\nu)_z$ for $\lambda = 0, .0005, .001$ and using $R = 2\pi/10$ and $L = 100$ (corresponding to a pitch length of $1\mu\text{m}$, front width of $.1\mu\text{m}$ and filament length $10\mu\text{m}$). This picture illustrates what we would expect to happen: the helix unwinds more at the upstream end than at the downstream end. We notice that the derivative of the perturbation is approximately a linear function, with a sinusoidal perturbation that comes from the particular solution part of $\hat{\theta}$. Physically, this term arises from a mismatch between the preferred configuration and the actual configuration.

4. NUMERICAL SIMULATIONS

In this chapter we describe the methods used to integrate equations (2.54) and (2.45), and present a representative set of results obtained.

The philosophy behind the numerical work was not to attempt to reproduce the Hotani experiment to the last detail, nor to perform an exhaustive categorisation of the behaviour of the equations over all of parameter space. Rather we were concerned with proving that the model described in Chapter 2 would suffice to produce the results obtained in experiments. We actually obtained surprisingly good quantitative agreement with experiment, using physically reasonable parameters.

4.1. Numerical methods

In this section we will describe the methods used to numerically integrate equations (2.45) and (2.54) which we rewrite here using the outer rescaling described in section 2.3 (suppressing hats).

$$\xi_\tau + u\xi_\alpha = -c_b(\xi_{\alpha\alpha} - e^{i\theta})_{\alpha\alpha} \quad (4.1)$$

$$\theta_\tau = -c_4\theta_{\alpha\alpha\alpha\alpha} + \theta_{\alpha\alpha}f''(\theta_\alpha/P) - c_c\text{Im}(e^{i\theta}\xi_{\alpha\alpha}^*) \quad (4.2)$$

The space domain will be taken to be $(0, L)$ where L is now measured in units of P , the pitch length (recall typically $P \sim 2\mu\text{m}$). We also rewrite the boundary conditions for convenience:

$$\begin{aligned} \xi(0) &= 0 & \xi_{\alpha\alpha}(0) &= 1 \\ \xi_{\alpha\alpha}(L) &= e^{i\theta(L)} & \xi_{\alpha\alpha\alpha}(L) &= i\theta_\alpha(L)e^{i\theta(L)} \\ \theta(0) &= 0 & \theta_{\alpha\alpha}(0) &= 0 \\ \theta_{\alpha\alpha}(L) &= 0 & c_4\theta_{\alpha\alpha\alpha}(L) &= f'(\theta_\alpha(L)) \end{aligned} \quad (4.3)$$

The energy functional f will be taken to be symmetric,

$$f(x) = -\frac{1}{2} \left(\frac{x}{2\pi} \right)^2 + \frac{1}{4} \left(\frac{x}{2\pi} \right)^4. \quad (4.4)$$

We shall impose the initial condition at $\tau = 0$ that the filament is at an energy minimum, that is $\theta_\alpha = 2\pi$ so

$$\theta(\alpha) = 2\pi\alpha \quad (4.5)$$

and $(\xi_{\alpha\alpha} - e^{i\theta}) = 0$ so

$$\xi(\alpha) = \frac{1}{(2\pi)^2} (1 - e^{2\pi i \alpha}). \quad (4.6)$$

The basic integration method we shall use is best described in the following way. We choose a time step Δt and, for brevity, write $\xi^n = \xi(n\Delta t)$ and $\theta^n = \theta(n\Delta t)$ at the n 'th time step. Write equations (4.1) and (4.2) as

$$\xi_\tau = g(\xi, \theta) \quad (4.7)$$

$$\theta_\tau = h(\xi, \theta) \quad (4.8)$$

and we will analyse methods for approximately advancing each function forward in time by one timestep as follows.

$$\xi^{n+1} = G(\xi^n, \theta^n) \quad (4.9)$$

$$\theta^{n+1} = H(\xi^n, \theta^n). \quad (4.10)$$

We shall represent ξ on a lattice of $N + 1$ points evenly spaced from 0 to L . The lattice spacing, $\Delta = L/N$. We will write the computed value of ξ at the lattice point m at time $n\Delta t$ as ξ_m^n .

We will break the bend equation into two pieces as follows:

$$\xi_\tau = L_1[\xi] - u\xi_\alpha \quad (4.11)$$

where L_1 is the linear operator defined by $L_1[\xi] = -c_b(\xi_{\alpha\alpha} - e^{i\theta})_{\alpha\alpha}$. Our method will be to split (4.11) by first advancing ξ in time according to L_1 and then by the advection piece. Suppose that for both pieces we know a scheme to update ξ from one timestep to the next if that piece was alone on the right-hand side. Say,

$$\xi^{n+1} = S_1(\xi^n, \Delta t) \quad (4.12)$$

$$\xi^{n+1} = S_2(\xi^n, \Delta t) \quad (4.13)$$

describes these two schemes. Then the operator splitting we shall use will be of the form

$$\begin{aligned} \xi^{n+1/2} &= S_1(\xi^n, \Delta t) \\ \xi^{n+1} &= S_2(\xi^{n+1/2}, \Delta t). \end{aligned} \quad (4.14)$$

Other splittings are certainly possible [48].

The method for working with $\xi_\tau = L_1[\xi]$ will closely follow the exact projection method described in section 2.1, equations (2.13-2.18) and (2.37 - 2.38) under the assumption that θ is constant.

We first find numerically the stationary solution ξ^s which solves

$$0 = (\xi_{\alpha\alpha}^s - e^{i\theta})_{\alpha\alpha} \quad (4.15)$$

with the inhomogeneous boundary conditions given above (4.3).

$$\xi^s(\alpha) = \int_0^\alpha \left(\int_0^{\alpha'} e^{i\theta(\alpha'')} d\alpha'' \right) d\alpha' \quad (4.16)$$

Now defining $\xi = \hat{\xi} + \xi^s$ we are left with the problem

$$\hat{\xi}_\tau = -c_b \hat{\xi}_{\alpha\alpha\alpha\alpha} \quad (4.17)$$

with homogeneous boundary conditions $\hat{\xi}(0) = \hat{\xi}_{\alpha\alpha}(0) = \hat{\xi}_{\alpha\alpha}(L) = \hat{\xi}_{\alpha\alpha\alpha}(L) = 0$ which is solved by a Fourier projection method as described by equations (2.13-2.18),

specifically,

$$\hat{\xi}^{n+1} = \sum_k \left(e^{-k^4 \Delta t} \int_0^L \bar{W}_k \hat{\xi}^n d\alpha \right) \quad (4.18)$$

where the basis functions $W_k(\alpha)$ satisfy $\partial^4 W_k / \partial \alpha^4 = l^4 W_k$ and the homogeneous boundary conditions and the bar on \bar{W}_k signifies that these are normalised. k are not the integers, rather they are a countable set of positive numbers found in the construction of the W_k (similar to equation (2.15)). The values of k run from 0 to some maximum value K in the program. As in the usual (trigonometric) discrete Fourier transform, the number of k -values chosen will be less than the lattice size N .

Naively one might ask, why can't we just write down some simple numerical scheme to solve the simple problem $u_t = -u_{xxxx}$, such as the forward-time central-space scheme

$$\frac{u_m^{n+1} - u_m^n}{\Delta t} = - \frac{u_{m+2}^n - 4u_{m+1}^n + 6u_m^n - 4u_{m-1}^n + u_{m-2}^n}{\Delta^4} \quad (4.19)$$

and simply choose small time and space steps? (4.19), which is obviously consistent with the equations, is order 1 in time and 2 in space, but the question is answered by looking at the stability requirements (recalling the Lax-Richtmeyer theorem that consistency plus stability for a finite difference scheme is equivalent to convergence). We perform a von Neumann analysis by taking a Fourier transform in space, that is, we write $u_m^n = g^n e^{im\phi}$, where g is the amplification factor at each step. Dividing (4.19) through by $g^n e^{im\phi}$ we get

$$g = 1 - \frac{\Delta t}{\Delta^4} (e^{-2i\phi} - 4e^{-i\phi} + 6 - 4e^{i\phi} + e^{2i\phi}) \quad (4.20)$$

$$= 1 - \frac{2\Delta t}{\Delta^4} (\cos 2\phi - 4 \cos \phi + 3) \quad (4.21)$$

$$= 1 - \frac{2\Delta t}{\Delta^4} \sin^4 \frac{\phi}{2} \quad (4.22)$$

We therefore have that $|g| < 1$ only if $\Delta t < \Delta^4$. This is a prohibitively big restriction on the choice of time-step Δt .

We must look for a better way of integrating. Two possibilities are to use a spectral (projection) method, as described above, or an implicit scheme (for example, a Crank-Nicolson scheme [49]). The fact that L_1 is self-adjoint with these boundary conditions is a strong indicator that we should use the spectral method. In integrating the twist equation, which is not self-adjoint, we will use the implicit scheme described below.

Numerically implementing the spectral method requires several steps. The W_k functions must be computed and stored appropriately before beginning the time integration. Then each time we need to advance ξ in time we follow the following procedure twice, (for the real and imaginary parts in turn):

1. Compute the lattice function ξ^s by integrating $e^{i\theta}$ twice.
2. Set $\hat{\xi}^n = \xi^n - \xi^s$
3. Compute the projections $\bar{\xi}_k^n = \int_0^L \bar{W}_k \hat{\xi}^n d\alpha$ for the k -values described above (from $k = 0$ to $k = K$).
4. Move the projections forward in time so $\bar{\xi}_k^{n+1} = e^{-c_b k^4 \Delta t} \bar{\xi}_k^n$ (from $k = 0$ to $k = K$).
5. Project back into real space: $\hat{\xi}^{n+1} = \sum_k \bar{\xi}_k^{n+1}$.
6. Add back the particular solution: $\xi^{n+1} = \hat{\xi}^{n+1} + \xi^s$.

We shall examine these steps in sequence.

• Construction of W_k

The functions W_k must have the form $W_k = A_k \sin k\alpha + B_k \cos k\alpha + C_k \sinh k\alpha + D_k \cosh k\alpha$ for some set of m . Using the boundary conditions we may immediately set $B_k = D_k = 0$. The remaining boundary conditions may be concisely

expressed as the matrix equation

$$\begin{pmatrix} -k^2 \sin kL & k^2 \sinh kL \\ -k^3 \cos kL & k^3 \cosh kL \end{pmatrix} \begin{pmatrix} A_k \\ C_k \end{pmatrix} = \begin{pmatrix} 0 \\ 0 \end{pmatrix} \quad (4.23)$$

which has a non-trivial solution only if $\tan kL = \tanh kL$. This equation produces an infinite set of values of k . The corresponding unnormalised eigenfunctions are

$$W_k = \left(\frac{\sinh kL}{\sin kL} \sin k\alpha + \sinh k\alpha \right). \quad (4.24)$$

There is also a zero unnormalised eigenfunction $W_0 = \alpha$. This corresponds to a net slope of ξ , and will be removed from the solution at each time step. (Physically, this means that the filament should line up as closely as possible with the flow direction.)

Computationally we must first find the non-zero solutions of $\tan kL = \tanh kL$ satisfying $0 < k \leq K$. This is a transcendental equation, but we know quite a lot about where its solutions will fall from graphing the two functions in figure 4.1.

There is one solution in each interval (say) $((3.2 + q\pi)/L, (4.0 + q\pi)/L)$ for each value $q = 1, 2, \dots$, and the solutions get increasing close to $(2q + 1)\pi/(4L)$ as q increases. Knowing the solution brackets in particular is very useful in this kind of nonlinear root-finding problem, as a simple bisection-type method is then guaranteed to converge (albeit slowly). Since we only have to compute the values of k once, the bisection method will suffice.

Armed with values of k we now compute the normalised function values \bar{W}_k at each lattice point and store these values. In principle, these function values are correct to arbitrary precision.

- **Finding** $\xi^s = \int_0^\alpha \int_0^{\alpha'} e^{i\theta} d\alpha$

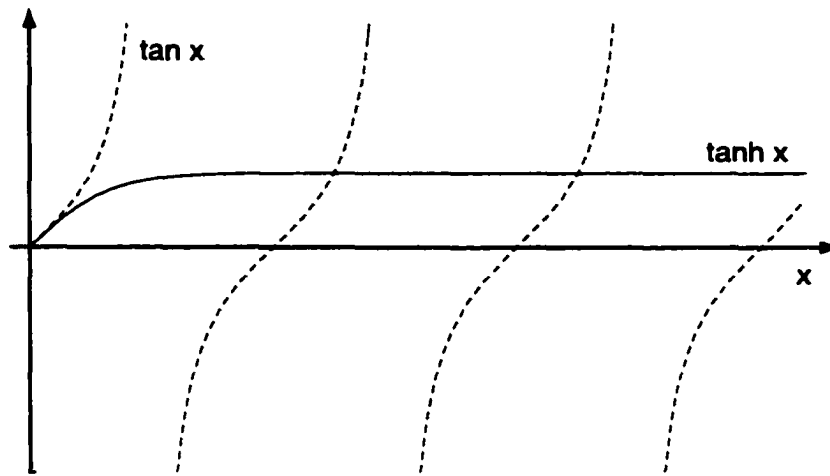


FIGURE 4.1. Tangent and hyperbolic tangent functions. The roots are distinct and as x increases, they become very close to the solutions of $\tan x = 1$.

It is a simple matter to use a numerical integration scheme twice [50] to compute ξ^s on the lattice, the only question is to estimate the error that arises. Let us rephrase the problem as

$$p(x) = \int_0^x q(x') dx' = \int_0^x \left(\int_0^{x'} r(x'') dx'' \right) dx' \quad (4.25)$$

where we know $r(x) = e^{i\theta}$ only at $N + 1$ lattice points evenly spaced from 0 to L and also that $q(0) = r(0) = 0$. Write p_m, q_m, r_m to represent the (exact) function values at each of the lattice points $m = 0, 1, \dots, N$.

Suppose we use a composite trapezoidal rule for both integrations. Then

$$q_m = \Delta \left(\frac{1}{2} r_m + \sum_{k=1}^{m-1} r_k \right) + e_m \quad (4.26)$$

where the error term, $e_m = O(m\Delta^3 r''(y))$ for some $0 < y < m\Delta$. e_m increases with m . Now in the process of summing up q_m to estimate p_m we can expect errors to arise from two sources - (i) the truncation error of the trapezoidal rule and (ii) the error e_m already contained within q_m . We therefore expect the error

in our estimate of p_m to be given by

$$E_m = O\left(m\Delta^3 q''(z) + \Delta \sum_{k=1}^m e_k\right) \quad (4.27)$$

for some new z . Bounding e_k above by $e_N = O(N\Delta^3 r''(y))$ and taking $i = N$ to find the worst error possible, we have

$$E_N = O(L\Delta^2 q''(z) + L^2\Delta^2 r''(y)) = O(\Delta^2) \quad (4.28)$$

provided the second derivative of r is well behaved (which it is in our problem). Using this method of two integrations to find ξ^s therefore introduces an error which scales at worst like $O(\Delta^2)$.

- **Computing the projections**

This involves performing one more numerical integration - that of $\hat{\xi}$ (which currently has an error of $O(\Delta^2)$) against the functions W_m (correct to high precision). This resulting error in the “Fourier” coefficients at step n , $\bar{\xi}_m^n$ remains $O(\Delta^2)$.

- **Move forward in time**

We now have ordinary differential equations for $k = k_0 \dots K$,

$$\frac{d}{dt}\bar{\xi}_k^n = -c_4 k^4 \bar{\xi}_k^n. \quad (4.29)$$

This equation is exactly integrable with solution $\bar{\xi}_k^{n+1} = e^{-c_4 k^4 \Delta t} \bar{\xi}_k^n$. No additional error is introduced at this point.

- **Project back into real space** The summation

$$\hat{\xi}^{n+1} = \sum_{k=k_0}^K \bar{\xi}_k^{n+1} \quad (4.30)$$

is in principle exact. However we should think of the terms neglected by choosing finite K . All components $\bar{\xi}_k$ for $m > K$ are set to zero at each time step. We

need to determine how much error is introduced by this approximation. The key point is that the high-frequency terms are being damped by their wavenumber to the fourth power. Therefore, for high enough K , the first neglected term has magnitude $\sim e^{-c_1 K_+^4 \Delta t}$ where $K_+ \simeq K + \pi$ is the next k -value after K . For small Δt , K can thus be chosen so that this term is comparable to the other errors arising in this scheme.

We have now completed the integration of $\hat{\xi}_t = L_1[\hat{\xi}]$, with accumulated error (for large enough K) of order Δ^2 in space and minimal error in time. Also, the number of operations is seen to scale linearly with N .

We can use the simplest possible advection scheme to work with $\xi_\tau = -u\xi_\alpha$, first order backward space - forward time:

$$\frac{\xi_m^{n+1} - \xi_m^n}{\Delta t} = -u \frac{\xi_m^n - \xi_{m-1}^n}{\Delta} \quad (4.31)$$

This scheme is obviously numerically consistent, and a very standard exercise in von Neumann analysis shows that it is stable provided $0 \leq u\Delta t/\Delta \leq 1$ [51]. Under this condition, then, the Lax-Richtmeyer theorem states that the scheme is convergent. The scheme is accurate of order 1 in space and 1 in time.

One can also consider higher order schemes for this problem, for example the forward-time central-space scheme

$$\frac{\xi_m^{n+1} - \xi_m^n}{\Delta t} = -u \frac{\xi_{m+1}^n - \xi_{m-1}^n}{\Delta} \quad (4.32)$$

which is order 2 accurate in space. This scheme applied to $\xi_\tau = -u\xi_\alpha$ is unstable. The question of whether (and if so, under what conditions) it is unstable in the simple splitting scheme (4.14) for $\xi_\tau = L_1[\xi] - \xi_\alpha$ remains. One may draw a comparison with the solution of the convection-diffusion equation $u_t = u_{xx} - au_x$ for which the central-space scheme

$$\frac{u_m^{n+1} - u_m^n}{\Delta t} = \frac{u_{m+1}^n - 2u_m^n + u_{m-1}^n}{\Delta^2} - a \frac{u_{m+1}^n - u_{m-1}^n}{\Delta} \quad (4.33)$$

turns out to be stable if $\Delta t/\Delta^2 \leq 1/2$. Both our equation and the convection-diffusion equation share a dissipative part with an advection. There is also the general slogan [48] that if we deal correctly with the highest derivative in the problem, using any consistent scheme for the lower derivatives will lead to a convergent scheme overall. The benefits of second-order accuracy in space (matching the spectral method described for L_1) make it worthwhile to implement both the central-space and backward-space methods and see what happens with each. We find in this case that it makes virtually no difference which scheme is used.

We now move to the development of a numerical scheme for the **twist equation**.

The twist equation (4.2) somewhat resembles the bend equation in that it contains a fourth-order space derivative. However, it is fundamentally nonlinear due to the contributions of $V''(\theta_\alpha)$ and $e^{i\theta}$.

The key to solving this equation will be to deal with the fourth derivative correctly. We might therefore try to build on the success of the projection method as follows. Write the equation as

$$\theta_\tau = -\theta_{\alpha\alpha\alpha\alpha} + N[\theta], \quad (4.34)$$

project onto appropriate normalised basis functions \bar{W}_k , calling the m 'th projection $\bar{\theta}_k$,

$$\frac{\partial}{\partial \tau} \int_0^L \theta \bar{W}_k d\alpha = - \int_0^L (\theta_{\alpha\alpha\alpha\alpha} + N[\theta]) \bar{W}_k d\alpha \quad (4.35)$$

and integrate by parts to obtain

$$\frac{d\bar{\theta}}{d\tau} = -k^4 \bar{\theta} + \int_0^L N[\theta] \bar{W}_k d\alpha \quad (4.36)$$

$$= -k^4 \bar{\theta} + \bar{N}. \quad (4.37)$$

We now integrate the first part exactly, and the second part to first order in time,

$$\bar{\theta}(\tau + \Delta t) = e^{-k^4 \Delta t} (\bar{\theta}(\tau) + \Delta t \bar{N}) + O(\Delta t) \quad (4.38)$$

and project back into real space by summing over all k .

This procedure is a very nice way to proceed for this kind of problem. However, we run into problems in constructing the basis functions W_k , which are the eigenfunctions of $\partial^4/\partial\alpha^4$ satisfying the boundary conditions $\theta(0) = \theta_{\alpha\alpha}(0) = \theta_{\alpha\alpha}(L) = 0$ and $c^4\theta_{\alpha\alpha\alpha}(L) = f'(\theta_\alpha(L))$. The final nonlinear boundary condition causes the problems. Without the inclusion of f in the free boundary condition, we will never be able to have a truly stress-free free end.

We must therefore look for another way of solving equation (4.2). We shall split the equation into two pieces (exactly as we did for the bend equation) by

$$\theta_\tau = N_1[\theta] + N_2[\theta] \quad (4.39)$$

where $N_1[\theta] = -\theta_{\alpha\alpha\alpha\alpha} + \theta_{\alpha\alpha}f''(\theta_\alpha/P)$ and $N_2[\theta] = -c_c\text{Im}(\mathbf{e}^{i\theta}\xi_{\alpha\alpha}^*)$. Our method will be to split (4.11) by first advancing θ in time according to N_1 and then N_2 .

Suppose that for both pieces we know a scheme to update θ from one timestep to the next if that piece was alone on the right-hand side. Say,

$$\theta^{n+1} = S_1(\theta^n, \Delta t) \quad (4.40)$$

$$\theta^{n+1} = S_2(\theta^n, \Delta t) \quad (4.41)$$

describes these two schemes. Then the operator splitting we shall use will be of the form

$$\begin{aligned} \theta^{n+1/2} &= S_1(\theta^n, \Delta t) \\ \theta^{n+1} &= S_2(\theta^{n+1/2}, \Delta t). \end{aligned} \quad (4.42)$$

We now set about finding methods to use as S_1 and S_2 .

As discussed above, the stability requirements on the time step necessary to use a simple explicit finite difference scheme such as (4.19) for the fourth-order piece of this equation are very restrictive. We therefore consider using a Crank-Nicolson type

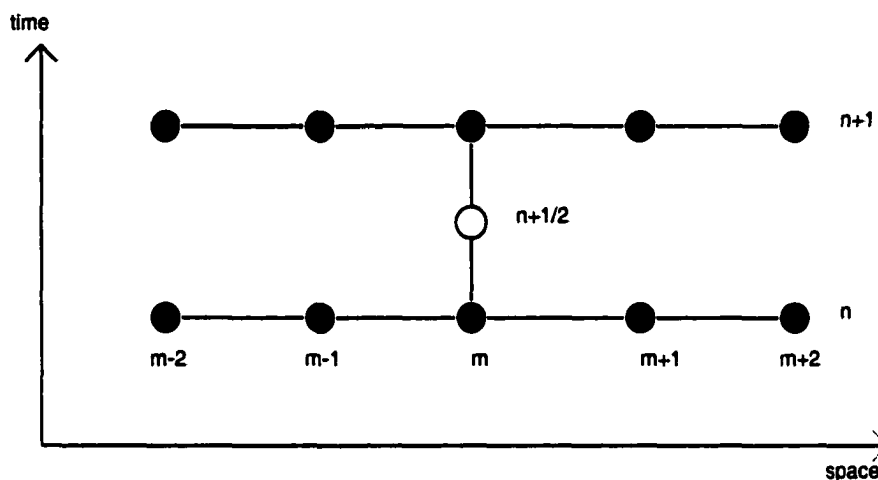


FIGURE 4.2. Computational stencil for fourth-order Crank-Nicolson. Space derivatives are taken at time steps n and $n + 1$, and averaged to make an estimate at the artificial step $n + 1/2$.

implicit method. The idea of Crank Nicolson is to evaluate the spatial derivatives at a point in time midway between τ and $\tau + \Delta t$ as shown in figure 4.2.

This leads to the following finite difference scheme:

$$\frac{\theta_m^{n+1} - \theta_m^n}{\Delta t} = -\frac{1}{2} \left(\frac{\theta_{m+2}^n - 4\theta_{m+1}^n + 6\theta_m^n - 4\theta_{m-1}^n + \theta_{m-2}^n}{\Delta^4} \right) - \frac{1}{2} \left(\frac{\theta_{m+2}^{n+1} - 4\theta_{m+1}^{n+1} + 6\theta_m^{n+1} - 4\theta_{m-1}^{n+1} + \theta_{m-2}^{n+1}}{\Delta^4} \right) \quad (4.43)$$

Similarly to the usual Crank-Nicolson scheme for the diffusion equation [51], this scheme is second order accurate in space and time, and we prove stability via von Neumann analysis by replacing the θ_m^n with the Fourier modes $g^n e^{im\phi}$:

$$g = 1 - \frac{\Delta t}{2\Delta^4} ((e^{2i\phi} - 4e^{im\phi} + 6 - 4e^{-im\phi} + e^{-2i\phi}) (1 + g)) \quad (4.44)$$

$$= \frac{1 - \frac{\Delta t}{\Delta^4} \sin^4 \frac{\theta}{2}}{1 + \frac{\Delta t}{\Delta^4} \sin^4 \frac{\theta}{2}} \leq 1 \quad (4.45)$$

The scheme is therefore unconditionally stable. Together with consistency (obvious) this shows that the method is convergent.

terms of an amplification factor g of a Fourier mode $e^{im\phi}$)

$$g = \frac{1 - 8\frac{\Delta t}{\Delta^4} \sin^4 \frac{\phi}{2} - 2\frac{f_m \Delta t}{\Delta^2} \sin^2 \frac{\phi}{2}}{1 + 8\frac{\Delta t}{\Delta^4} \sin^4 \frac{\phi}{2} + 2\frac{f_m \Delta t}{\Delta^2} \sin^2 \frac{\phi}{2}} = \frac{1 - y}{1 + y} \quad (4.55)$$

$$y = 2\frac{\Delta t}{\Delta^2} \sin^2 \frac{\phi}{2} \left(\frac{4}{\Delta^2} \sin^2 \frac{\phi}{2} + f_m \Delta t \right) \quad (4.56)$$

Using $f''(x) = (3x^2/(2\pi)^2) - 1$ (the second derivative of (4.4)) we find that $f_m > -1$. But any negative value of f_m , means $y < 0$ for small values of ϕ regardless of the choice of Δ and so we have shown that $|g|$ is not bounded above by 1. If this stability analysis were the correct one for the problem at hand, this would be catastrophic as then the growth of a mode $e^{i\phi}$ would grow exponentially with the number of time-steps, so as Δt was decreased the behaviour over fixed time would get worse! (The true behaviour of $\theta_\tau = -\theta_{\alpha\alpha\alpha\alpha} + A\theta_{\alpha\alpha}$ is governed by the dispersion relation where a mode of wavenumber k grows at a rate $\sigma(k) = -k^4 - Ak^2$ so if A is negative, there is a linearly excited band of low-frequency modes $0 < k < \sqrt{A}$.)

Numerical experiments using the scheme (4.52) to solve the *nonlinear* equation (2.45), however, show good convergence properties (and certainly not low-frequency blow-up). We have not proved that the solution converged to is the correct solution. However, if the approximate steady solution $\theta_\alpha = 2\pi \tanh(\alpha/\sqrt{2})$ is used as the initial condition, it is held fixed by the scheme and is stable to applied perturbations. Similarly, we have tested that the constant steady solution $\theta_\alpha = 2\pi$ is stable to perturbations. It has been proven [52] that consistent, numerically convergent finite difference schemes for well-posed hyperbolic (which this is not) equations are in fact converging to the right thing, and the same is believed to be true for parabolic equations. Our equations are neither hyperbolic nor parabolic, but these facts give us confidence that the scheme is performing correctly.

The discussion of the integration of the twist equation is completed by dealing with the forcing term $e^{i\theta} \xi_{\alpha\alpha}^*$. This is just a non-linear O.D.E.-type term in θ . We

estimate $\xi_{\alpha\alpha}^*$ using a central difference approximation and take an Euler step forward:

$$\frac{\theta_m^{n+1} - \theta_m^n}{\Delta t} = e^{i\theta_m^n} \left(\frac{\xi_{m+1}^{*n} - 2\xi_m^{*n} + \xi_{m-1}^{*n}}{\Delta^2} \right) \quad (4.57)$$

A quick check shows that this approximation is accurate to first order in time and second in space.

4.2. Numerical results

We present numerical results using biologically realistic parameters in three cases: (i) flow velocity below that sufficient to cause a polymorphic transition at the fixed end, (ii) flow velocity close to critical, and (iii) flow velocity somewhat above the critical velocity.

The following parameters were used (refer to the discussion of section 2.4 for details): $\zeta_{\perp} = 1\text{g}/(\text{cm s})$, $\zeta_R = 10^{-13}\text{g cm/s}$, $A = 10^{-15}\text{erg cm}$, $H = 2 \times 10^{-7}\text{erg/cm}$, $P = 2\mu\text{cm}$, $L = 20\mu\text{m}$ and $\Omega_2^0 = 25000/\text{cm}$ (corresponding to a flagellar radius of $1\mu\text{m}$), corresponding to dimensionless parameters (from section 2.3) of $c_b = .041$, $c_c = 120$ and $c_4 = .02$ (corresponding to a front width of 200nm). The potential chosen was the quartic function described by (2.56). Therefore, we are considering a filament with two exactly opposite stable states. The initial state used was entirely in the left-handed helical preferred state.

All simulations presented were performed using a time-step of $\Delta t = .0002$ and a 400 - point spatial mesh, with 8 seconds of real time taking about 30 hours of machine time on a 433 MHz single-processor machine. Shorter convergence checks were performed using finer time and space meshes to prove that the meshes used for these figures are sufficient for our purpose.

The minimum flow speed determined to cause polymorphism using these parameters was within 1% of $10\mu\text{m/s}$. The comparable speed in Hotani's experiment was estimated to be of the order of $1\mu\text{m/s}$.

We saw that if the forcing flow velocity was too slow ($U < 10\mu\text{m/s}$), no polymorphism occurred. The twist rate, however, did indicate a winding-up of the helix at the fixed end (figure 4.3). On increasing the forcing flow speed to the critical value, fronts were nucleated at the fixed end and propagate to the free end (figures 4.4, 4.5 and 4.6). Using these parameters, we observed two opposing fronts on the filament at one time, as in the actual experiments. At $U = 13\mu\text{m/s}$, somewhat beyond the critical flow speed (figures 4.7, 4.8 and 4.9), we observe that up to three fronts may exist on the helix at one time, linking up to four regions of opposite handedness. Much beyond this level of fluid stress, the number of different regions becomes very large, simulation of the filament becomes quite erratic. At this point, although the numerical results are still convergent, we doubt that the assumptions made in building the model are still qualitatively correct.

We also make two graphs illustrating general behaviours of the filament over a range of flow speeds. The first (figure 4.10) illustrates that the increase in the long-time rate of nucleation of handedness transformations with increased fluid stress is by no means simple to determine. The second (figure 4.11) validates the scaling analysis performed on page 44 by plotting the speed of the first invading transition against the applied fluid flow speed. The agreement is quite striking, and strongly suggests that the scaling result (depending solely on the geometry of the helix) is correct.

We summarise as follows:

- Below a critical velocity of applied flow speed, the helix unwinds slightly from the preferred state to reach a steady state.
- Above the critical velocity we observe nucleation, propagation and resetting of domains of different handedness on the filament. The critical velocity obtained using physically reasonable parameters ($10\mu\text{m/s}$) is close to the estimate of Hotani (a few $\mu\text{m/s}$). We believe that with some small modification of the parameters, we could obtain even better agreement.

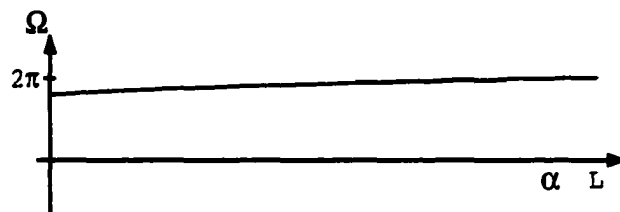


FIGURE 4.3. Steady twist-rate plot for flow speed less than critical. After a few seconds of real time, for flow speeds below critical, we find that the filament twist rate (Ω), while remaining in the preferred state at the free (right-hand) end, takes on a monotonic profile with a minimum twist rate at the pinned (left-hand) end. This is in agreement with our intuition regarding the spatial variation of torque on the filament, and the asymptotic result of section 3.2.

- The speed at which a front in Ω traverses the filament grows with the applied fluid velocity. The scaling result (page 44) is validated.
- The frequency of nucleation of fronts and the number of fronts on the filament at one time increases non-trivially with the flow speed.

Oscillations in the plots of Ω are observed, which look at first glance like artifacts arising from the numerical scheme used. In fact, they appear to be real behaviour of the system, and are probably far-from-equilibrium developments of the near-equilibrium oscillations found in section 3.2.

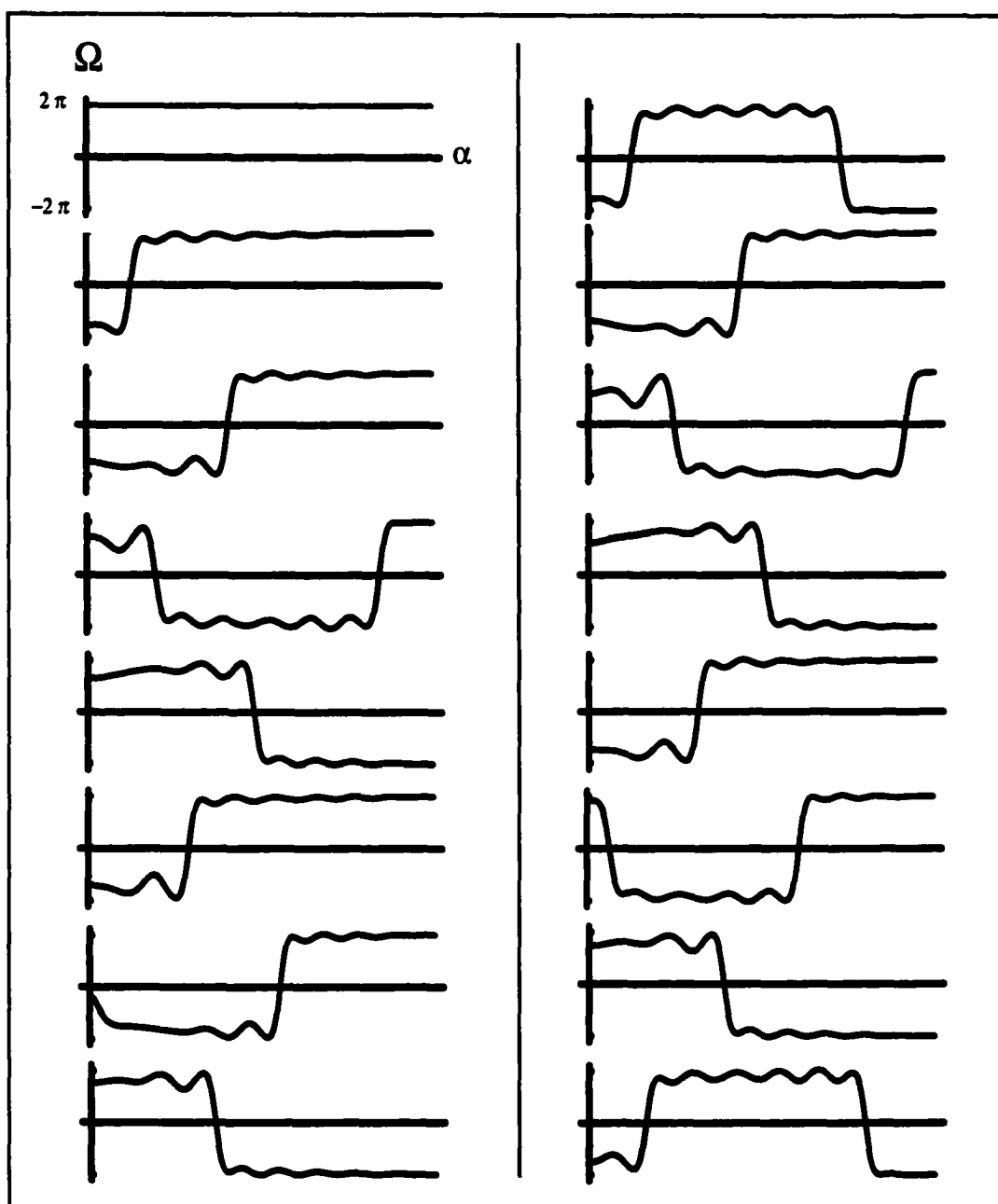


FIGURE 4.4. Time series of Ω plots for flow speed close to critical ($U=10\mu\text{m/s}$). Time runs from top left ($t=0\text{s}$) to bottom left, then top right to bottom right ($t=25\text{s}$), corresponding to a frequency of about .3 Hz for nucleation (handedness change) events at the pinned end. First column matches the configuration diagrams of figure 4.6.

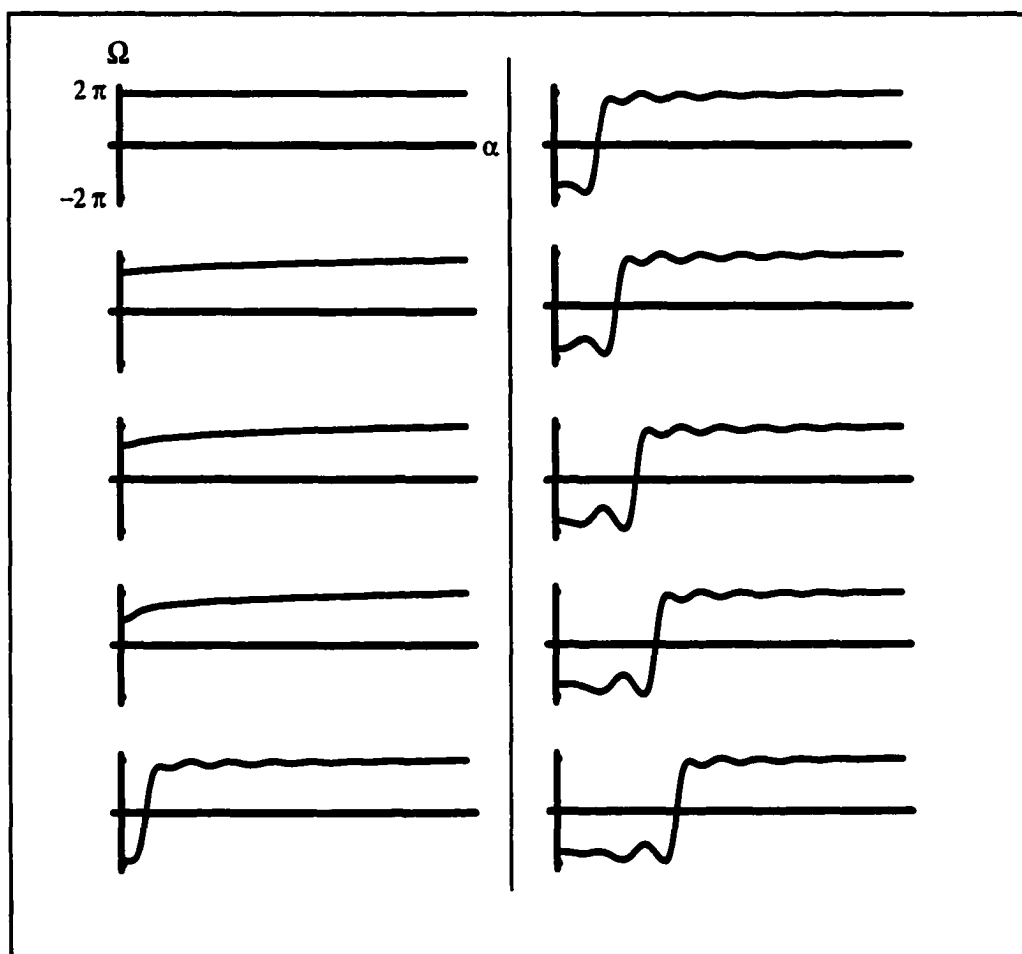


FIGURE 4.5. Detailed initial time series of Ω plots for flow speed close to critical ($U=10\mu\text{m/s}$). Time runs from top left ($t=0\text{s}$) to bottom left, then top right to bottom right ($t=3\text{s}$). We observe an initially gentle change to the slope of $\Omega(z)$, until $\Omega(0)$ reaches the critical value, nucleating a sudden handedness change which then advances.

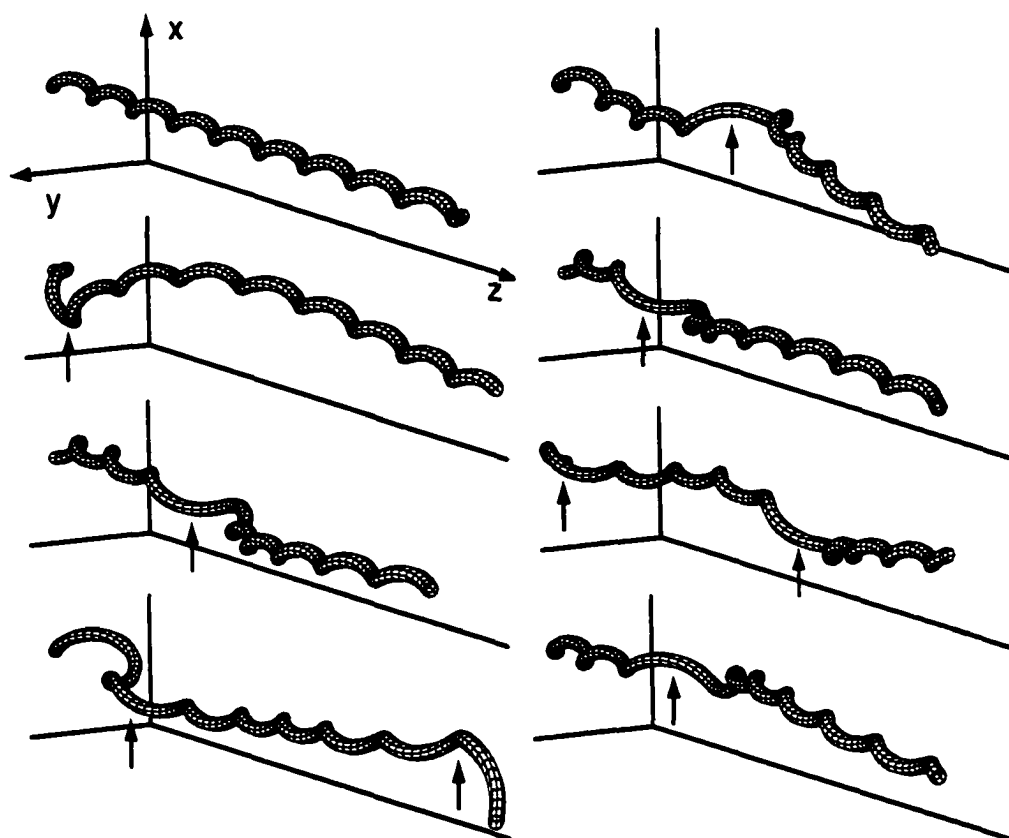


FIGURE 4.6. Filament configuration times series for flow speed close to critical ($U=10\mu\text{m/s}$). Again, time runs from top left ($t=0\text{s}$) to bottom left, then top right to bottom right ($t=11.7\text{s}$). Figures correspond exactly to the first column of figure 4.4. Arrows indicate points at which the handedness changes.

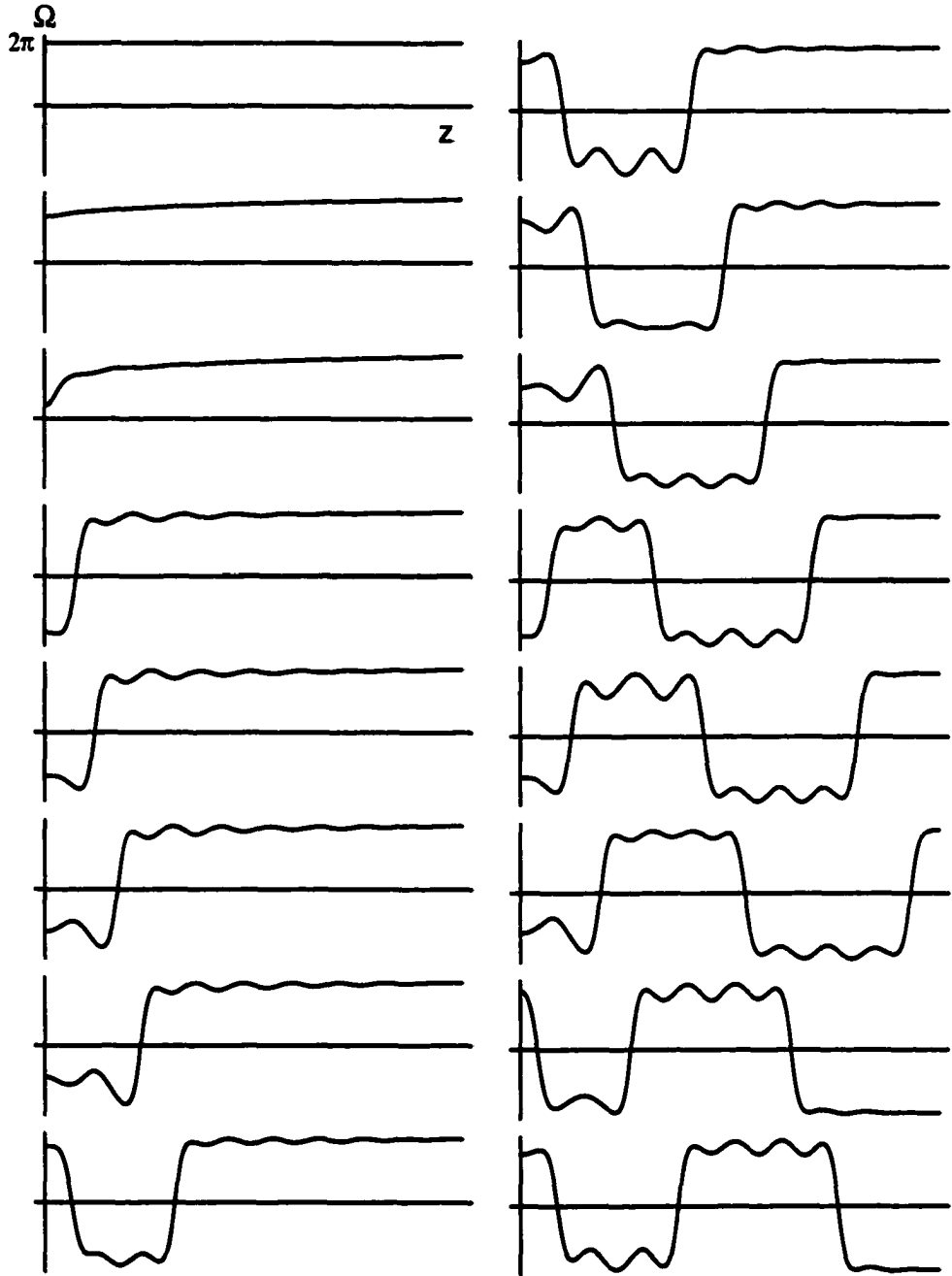


FIGURE 4.7. Time series of Ω plots for flow speed somewhat above critical ($U=13\mu\text{m/s}$). Time runs from top left ($t=0\text{s}$) to bottom left, then from top right to bottom right ($t=2.5\text{s}$). We see nucleation of a polymorphic front, quickly followed by an opposing front, and so on. Notice that the regions of a single handedness are narrower than in figure 4.4, and the fronts joining them move more quickly.

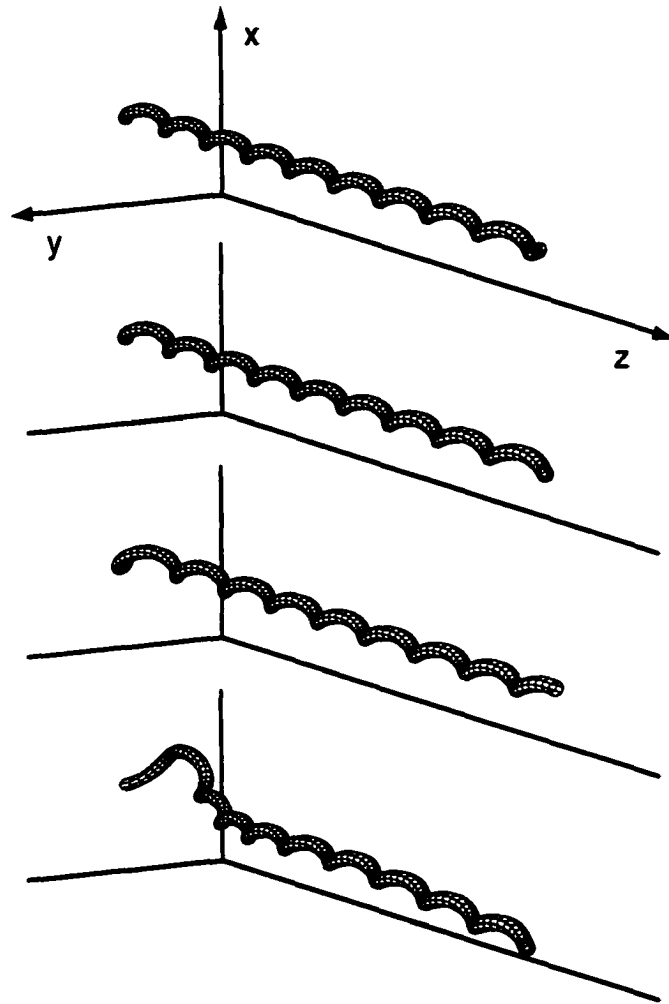


FIGURE 4.8. Short-time filament configuration times series for flow speed somewhat above critical ($U=13\mu\text{m/s}$). Time runs from top ($t=0\text{s}$) to bottom (0.5s). Observe the slow unwinding of the helical shape and then the sudden jump to an opposing handed state at the pinned end.

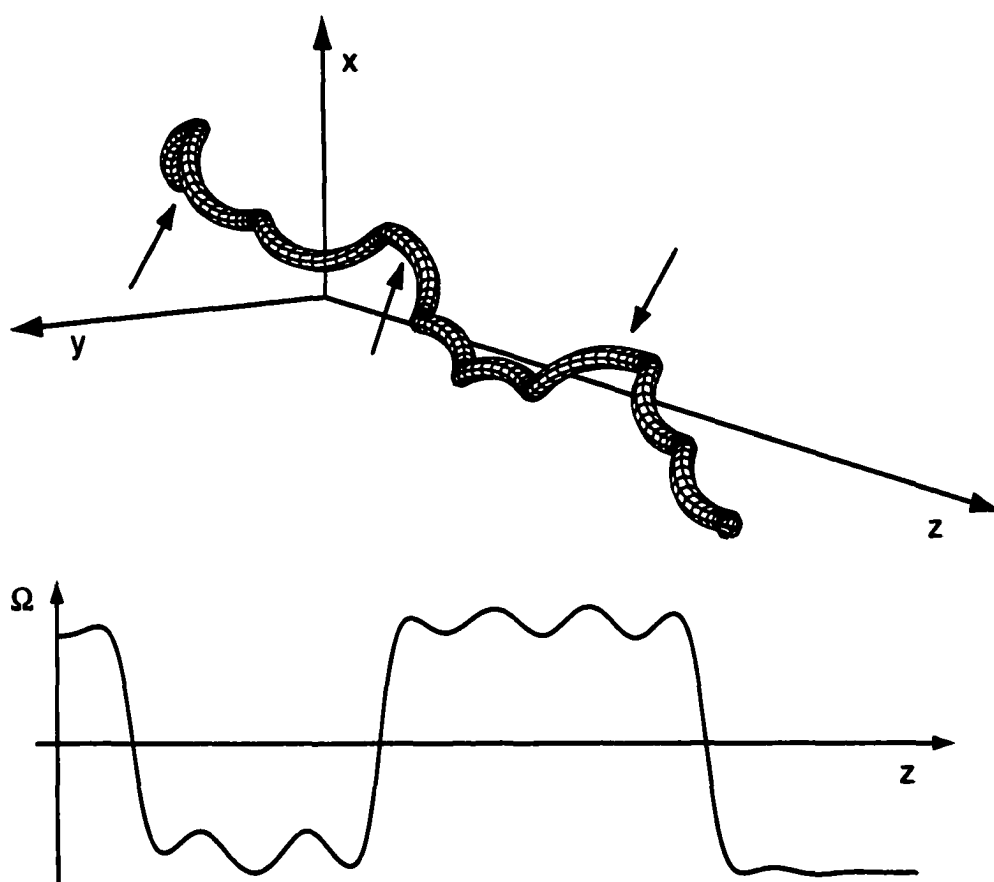


FIGURE 4.9. Snapshot of filament configuration for flow speed somewhat above critical ($U=13\mu\text{m/s}$). We illustrate the relationship between Ω and the configuration in this plot. The lower plot of Ω is identical to the last plot in the time series of figure 4.7. Arrows point out the chirality switching points, which are not really obvious any more. Above $U=13\mu\text{m/s}$, it becomes increasingly difficult to distinguish regions of different handedness.

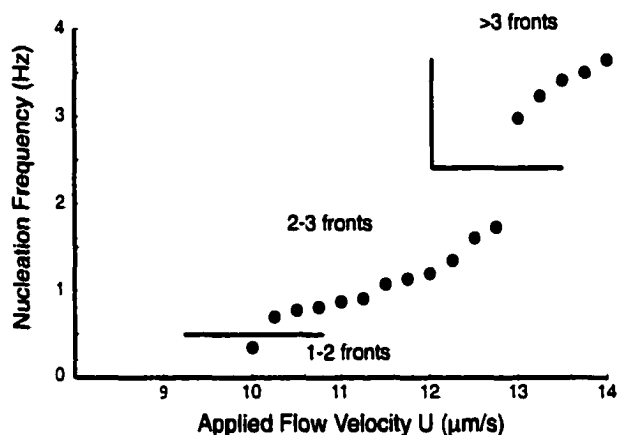


FIGURE 4.10. Chirality transition frequency as a function of imposed fluid stress. Plot shows the frequency of chirality transitions against the imposed fluid speed. The number of inversions on the filament at any one time is also indicated. Note strongly nonlinear behaviour in the inversion frequency.

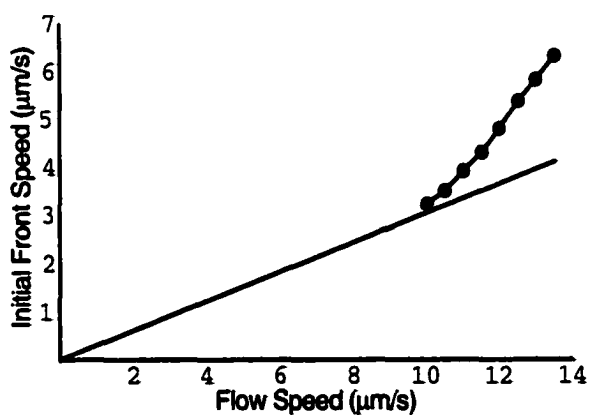


FIGURE 4.11. Initial front velocity against applied fluid flow speed. Dots indicate experimentally determined velocities for the speed of invasion of the first front nucleated. The solid line indicates the scaling result (equation (2.75)), valid only near onset ($U = 10\mu\text{m/s}$). The agreement is striking.

5. CONCLUDING REMARKS

The main goal of this dissertation was to present a theoretical explanation of the Hotani experiment, beyond the level of vague statements about torques and twist rates. The model presented in Chapter 2.1 does, as proven by the numerical results given in Chapter 4, produce quantitatively and qualitatively similar features to those observed by Hotani. Additionally, by using physically realistic parameters, we obtain some quantitative agreement with experiment. This suggests strongly that the approximations made are peripheral, and do not affect the fundamental dynamics.

As an example of a development of this theory we mention the recent observation of Berg et al. [53] that a flagellum rotating near a solid wall is observed to straighten. We can heuristically explain this result within the framework described here by noting that a straight filament rotates much more easily than a helix. We therefore propose to add a term to the energy V of the rotating flagellum of the form $M\Omega^2$ where the factor M will depend on the distance of the filament from the wall, the speed of rotation and elastic and geometric properties of the flagellum. As the distance to the wall decreases, M must increase. We therefore picture the minima of the bistable potential V becoming shallower, and coming closer to $\Omega = 0$, a straight filament, until they may finally merge close to $\Omega = 0$.

The principal approximation made in deriving the equations of motion was to change from the (intrinsic) arc length coordinate s to (external) (x, y, z) coordinates. The position of the filament was then given by two functions $X(z)$ and $Y(z)$. We then rewrote the strains Ω_1 and Ω_2 approximately in terms of second derivatives of these functions and to quadratic order in the slopes X_z and Y_z . The equations of motion for a bistable helix relaxing can be exactly formulated in terms of s [23], and include several terms not included here (for instance, writhe-tracking). To add the forcing fluid flow would not be difficult to implement in a computer simulation. The

second approximation was to approximate the forcing flow as a uniform drag in the z direction. As discussed in Chapter 2 (page 38) it would be a much more difficult proposition to properly model the interaction between the filament and the flow. It is questionable how much additional insight one could gain by removing these two approximations and performing simulations.

The natural next step in the study of flagellar dynamics, therefore, would be to perform a sequence of optical trapping experiments, probably using fluorescently labelled flagella [16].

1. A reproduction of Hotani's experiments using a trapped bead as the anchor point. This would remove variations in the forcing flow caused by the presence of the slide.
2. Use of magnetic beads [54] on either one or both ends of the filament to apply a torque to the flagellum with a free and fixed end. This will clear up issues regarding whether the extensive strain on the flagellum is important in the Hotani experiment, and permit elucidation of the shape of the twist-rate potential V .
3. Observation of the interaction between multiple pinned flagella under an imposed flow. This will give insight into the bundling - unbundling transition in swimming cells, although under extensive rather than compressive circumstances.

None of these experiments should be particularly difficult to perform using modern laser-trapping techniques.

A. LOW REYNOLDS NUMBER HYDRODYNAMICS

In this appendix I will outline the construction of two of the fundamental singularities of stokes flow, and then use them to determine the flow-field due to a ‘moving cylindrical flagellum’ in the low Reynolds number regime, in the cases where (i) it is in an unbounded fluid and (ii) it is sticking out from an infinite wall at 90° and rotating. I will also estimate the drag on a nearby ‘cylindrical flagellum’ using biologically relevant parameters, under each of the calculated flows.

A.1. Fundamental singularities

Throughout we will assume the equations of *incompressible Stokes flow* are the appropriate approximation to the Navier Stokes equations:

$$\nabla \cdot \mathbf{u} = 0 \tag{A.1}$$

$$\nabla p = \mu \nabla^2 \mathbf{u} + \mathbf{F}(\mathbf{x}) \tag{A.2}$$

where μ is the viscosity, \mathbf{u} the fluid velocity vector and p the pressure. $\mathbf{F}(\mathbf{x})$ is the applied force at \mathbf{x} . By taking the divergence of (A.2) we find that

$$\nabla^2 p = 0 \tag{A.3}$$

and that

$$\nabla^4 \mathbf{u} = 0 \tag{A.4}$$

if there is no force applied.

We now proceed to derive the *Stokeslet*, a fundamental singularity of Stokes flow.

We build \mathbf{F} up from point forces of the form $\mathbf{F}\delta(\mathbf{r})$ of force per unit volume, \mathbf{r} is the vector displacement from the point of application of the force \mathbf{F} . Thus, with a

single point force applied, we find that

$$\nabla^2 p = \nabla \cdot (\mathbf{F} \delta(\mathbf{r})) \quad (\text{A.5})$$

which has solution

$$p = -\nabla \cdot (\mathbf{F}/4\pi r). \quad (\text{A.6})$$

This is a classical dipole field.

We will determine the velocity field when $\mathbf{F} = (F, 0, 0)$. Then (A.6) becomes $p = Fx/4\pi r^3$ and therefore,

$$\nabla^2 \mathbf{u} = \frac{1}{\mu} \nabla p = \frac{F}{4\pi\mu} \left(\frac{1}{r^3} - \frac{3x^2}{r^5}, \frac{-3xy}{r^5}, \frac{-3xz}{r^5} \right). \quad (\text{A.7})$$

and it can be checked that

$$\mathbf{u} = -\frac{1}{6} r^2 \left(\frac{F}{4\pi\mu} \nabla \frac{x}{r^3} \right) \quad (\text{A.8})$$

is one solution. But we can add a vector $(F/6\pi\mu r, 0, 0)$ to this \mathbf{u} without altering its harmonicity (as $1/r$ is harmonic), and this yields the solution

$$\mathbf{u} = \frac{F}{8\pi\mu} \left(\frac{x^2 + R^2}{r^3}, \frac{xy}{r^3}, \frac{xz}{r^3} \right) \quad (\text{A.9})$$

$$p = \frac{Fx}{4\pi r^3}. \quad (\text{A.10})$$

For a more general \mathbf{F} we have the equivalent tensor notation results:

$$u_i = \frac{F_j}{8\pi\mu} \left(\frac{\delta_{ij}}{r} + \frac{r_i r_j}{r^3} \right) \quad (\text{A.11})$$

$$p = \frac{F_j r_j}{4\pi r^3}. \quad (\text{A.12})$$

We can now proceed to build up force distributions using the linearity of the Stokes equations in an unbounded fluid. Under the additional assumption that \mathbf{F} is solenoidal, i.e., $\nabla \cdot \mathbf{F} = 0$, we can write

$$\mathbf{F}(\mathbf{x}) = 4\pi\mu \nabla \times \boldsymbol{\Omega}(\mathbf{x}) \quad (\text{A.13})$$

where $\mathbf{\Omega}$ is now a vector potential with dimensions of vorticity. Let us take $\mathbf{\Omega}(\mathbf{x}) = \mathbf{G}\delta(\mathbf{x})$ to represent a point source of vorticity. The related velocity is now

$$\nabla^2 \mathbf{u} = -4\pi \nabla \times (\mathbf{G}\delta(\mathbf{x})). \quad (\text{A.14})$$

It can be checked that the solution is

$$\mathbf{u} = \nabla \times \left(\frac{\mathbf{G}}{r} \right) = \frac{\mathbf{G} \times \mathbf{x}}{r^3} \quad (\text{A.15})$$

and we refer to this velocity profile as a *rotlet*. This point source of vorticity can also be found by taking the antisymmetric part of the gradient of a stokeslet. [55] The vorticity of the rotlet is:

$$\zeta = \nabla \times \mathbf{u} = -\frac{\mathbf{G}}{r^3} + \frac{3(\mathbf{G} \cdot \mathbf{x}) \mathbf{x}}{r^5} \quad (\text{A.16})$$

Physically, the velocity field due to a rotlet is exactly the same as that generated by a sphere of radius a rotating about \mathbf{G} with angular velocity $\omega = |\mathbf{G}|/a^3$, since it satisfies the no-slip boundary condition $\mathbf{u} = \omega \times \mathbf{x}$ at $r = a$. It therefore makes sense to use line distributions of rotlets to build flow fields for rotating cylindrical objects. We should also note that the pressure field associated with a rotlet is uniform.

A.2. Flow field due to a rotating cylinder

The idea is to build a line distribution of rotlets along the major axis of the cylinder. The strength of the distribution need not be uniform. We begin by taking the distribution to be of strength $\Gamma(x)$ along the x -axis, from $x = -c$ to $x = c$. If we do this, then the tangential fluid velocity at a point (x, r, θ) will be

$$\mathbf{u}_\theta = r \int_{-c}^c \frac{\Gamma(\xi) d\xi}{((x - \xi)^2 + r^2)^{3/2}}. \quad (\text{A.17})$$

We ‘match’ the fluid velocity to the rotation of an axisymmetric body of shape $r = r_0(x)$ rotating at rate ω (assumed uniform along the body) by

$$\omega = \int_{-c}^c \frac{\Gamma(\xi) d\xi}{((x - \xi)^2 + r_0(x)^2)^{3/2}}. \quad (\text{A.18})$$

We have several degrees of freedom - we can specify c , $\Gamma(x)$ and $r_0(x)$. But to match all three to sensibly represent a solid body rotating around the x -axis is in general a difficult problem. We begin with a series of simple cases.

To begin with, we set $c = \infty$ and $\Gamma(x) = \Gamma$ independent of x . The shape is taken to be a uniform cylinder $r_0(x) = a$ rotating at an angular velocity ω . We must satisfy the no-slip condition

$$\omega = \Gamma \int_{-\infty}^{\infty} \frac{d\xi}{((x - \xi)^2 + a^2)^{3/2}}. \quad (\text{A.19})$$

This is easily done, to get $\Gamma = a^2\omega/2$. We therefore find the following general result for the fluid flow at a point at distance r from the x -axis,

$$u_\theta(x, r) = r \frac{a^2\omega}{2} \int_{-\infty}^{\infty} \frac{d\xi}{((x - \xi)^2 + r^2)^{3/2}} = \frac{a^2\omega}{r} \quad (\text{A.20})$$

To attack the problem of the finite slender cylinder, we first accept that it will be difficult to work with a true cylinder. However, following exactly the approach taken by [56] we can find analytical results for shapes very close to true slender cylinders.

We will consider again a uniform strength distribution of rotlets along the x -axis, extending from $-c$ to c . $2c$ is not necessarily the length of the cylinder! The no-slip condition (A.19) is now integrable to give

$$\omega = \frac{\Gamma}{r_0(x)} \left(\frac{x + c}{((x + c)^2 + r_0(x))^{1/2}} - \frac{x - c}{((x - c)^2 + r_0(x))^{1/2}} \right) \quad (\text{A.21})$$

for some shape $r_0(x)$ which we do not yet know. We will now specify two points $(x = 0, r = b)$ and $(x = a, r = b)$ on the shape. Using (A.21), this means that

$$2ac(a^2 - c^2)^{-2} = \omega/\Gamma \quad (\text{A.22})$$

$$2cb^{-2}(b^2 + c^2)^{-1/2} = \omega/\Gamma. \quad (\text{A.23})$$

From this we can find the shape function r_0 as an expansion when b/a is small,

$$\frac{r_0}{b} = 1 - \left(\frac{b}{c}\right)^2 \frac{x^2(3c^2 - x^2)}{4(c^2 - x^2)^2} + O(b/c)^4 \quad (\text{A.24})$$

and an expansion for c :

$$\frac{c}{a} = 1 - \frac{b}{2a} - \frac{7}{64} \left(\frac{b}{a}\right)^3 + O(b/a)^4. \quad (\text{A.25})$$

It turns out that this shape is extraordinarily close to a slender plane cylinder for $(\frac{b}{a})$ small. We can now compute $u_\theta(x, r)$:

$$\begin{aligned} u_\theta(x, r) &= r\Gamma \int_{-c}^c \frac{d\xi}{((x-\xi)^2 + r^2)^{3/2}} \\ &= \frac{\Gamma}{r} \left(\frac{x+c}{((x+c)^2 + r^2)^{1/2}} - \frac{x-c}{((x-c)^2 + r^2)^{1/2}} \right) \end{aligned} \quad (\text{A.26})$$

Having found the flow field around a finite-length rotating cylinder it is now possible to use an *image method* to obtain the flow for a cylinder perpendicular to an infinite plane wall (the y - z plane). The distribution of rotlets used will be from $x = -2c$ to $x = 2c$ and now the rotlet strength Γ will be positive for $x > 0$ and negative for $x < 0$.

There is an issue of whether the pressure continues to vanish when we introduce a planar wall, and whether this means we need to introduce other singularities to deal with this fact. But, by following the procedure in [55] where the tensor form for the pressure due to a rotlet with a wall is written down, it is found that the image singularity for a rotlet perpendicular to a wall is simply a rotlet of opposite sign.

After performing an integration analogous to (A.20), we find the flow field at a distance r from the centreline $x = 0$ to be

$$\begin{aligned} u_\theta &= -\frac{\Gamma}{r} \left(\frac{(x+c)}{((x+c)^2 + r^2)^{1/2}} \right. \\ &\quad \left. - \frac{2x}{(x^2 + r^2)^{1/2}} + \frac{(x-c)}{((x-c)^2 + r^2)^{1/2}} \right) \end{aligned} \quad (\text{A.27})$$

A.3. Application to modelling bacterial flagella

The general approach here will be to first calculate the magnitude of the flow field due to the first rotating cylindrical flagellum as a function of r , the distance from its

centreline. We will then place another, *non-rotating* cylindrical flagellum parallel to the original in this flow field and imagine that it has no impact on the flow field, and calculate the force on the flagellum using the drag law from Keller and Rubinow [37]. This is a fairly gross approximation, but it should serve to give some intuition into the force scales involved.

We will take the length of the flagellum to be $L = 15\mu\text{m}$ and the diameter to be $a = 20\text{nm}$. We will compute the drag on the passive flagellum at distances between centres of 30nm, 100nm and $1\mu\text{m}$. 30nm is rather close, even in the bundle. 100nm is a reasonable separation within the bundle and a micron is a reasonable 'resting' separation. The rotating flagellum will be taken to spin at 100Hz.

The drag law we'll use is $f_d = \zeta u$, with ζ given by [37].

$$\zeta = \frac{4\pi\mu L}{\log(L/a) - 0.5 + \log 2 - (1 - \frac{\pi^2}{2})/\log(L/a)}. \quad (\text{A.28})$$

We find from simple substitution into (A.25) that $c \simeq 7.45\mu\text{m}$. (A.24) yields

$$r_0 \simeq 10^{-6} - 4.5 \frac{x^2 (1.66 \times 10^{-6} - x^2)}{(5.6 \times 10^{-7} - x^2)^2} \quad (\text{A.29})$$

We use (A.22) to find $\Gamma = 3.14 \times 10^{-10}$. We use (A.26) to compute a maximal strength of flow at $(x = 0, r)$ as

$$u_\theta^M = \frac{4.7 \times 10^{-13}}{r\sqrt{5.5 \times 10^{-7} + r^2}} \quad (\text{A.30})$$

At 30nm separation this gives $u_\theta = 2.1\mu\text{m/s} \rightarrow 5 \times 10^{-9}\text{dyne} = .05\text{pN}$.

At 100nm separation this gives $u_\theta = .63\mu\text{m/s} \rightarrow 2 \times 10^{-9}\text{dyne} = .02\text{pN}$.

At $1\mu\text{m}$ separation this gives $u_\theta = .063\mu\text{m/s} \rightarrow 2 \times 10^{-10}\text{dyne} = 0.002\text{pN}$.

Now we consider the case of two rotating cylinders attached to a wall. As above, we take $c = 7.45\mu\text{m}$. The distribution of rotlets is taken to extend from $x = 0$ to $x = 2c$. We must still match the flow field to the no-slip boundary condition on the cylinder. This is done by matching at the point $x = c, r = b$. We find $\Gamma = \pi \times 10^{-10}$.

We can now find a table of values similar to those given above: (here, u_θ is averaged along the length of the passive flagellum).

At 30nm separation : $u_\theta = 2.0\mu m/s \rightarrow 5 \times 10^{-9} \text{dyne} = .05 \text{pN}$.

At 100nm separation : $u_\theta = .62\mu m/s \rightarrow 2 \times 10^{-9} \text{dyne} = .02 \text{pN}$.

At $1\mu m$ separation : $u_\theta = .059\mu m/s \rightarrow 1 \times 10^{-11} \text{dyne} = 0.001 \text{pN}$.

The notable thing is that the presence of the wall really makes very little difference to these figures.

REFERENCES

- [1] Whitman, W.B., Coleman, D.C. & Wiebe, W.J. Prokaryotes: the unseen majority. *Proc. Nat. Acad. Sci* **95**, 6578-6583 (1998).
- [2] Hotani, H. Micro-video study of moving bacterial flagellar filaments, III. Cyclic transformation induced by mechanical force. *J. Mol. Biol.* **156**, 791-806 (1982).
- [3] Berg, H. & Purcell, E.M. Physics of chemoreception. *Biophys. J.* **20**, 193-219 (1977).
- [4] see, for example Bustamante, C., Keller, D. & Oster, G. The physics of molecular motors *Accounts of Chemical Research* **34**, 412-420 (2001)
- [5] Namba, K. & Vonderviszt, F. Molecular architecture of bacterial flagellum. *Quart. Rev. Biophys.* **30**, 1-65 (1997).
- [6] Magariyama, Y. et al. Very fast flagellar rotation. *Nature* **371**, 752.
- [7] Tsang, N., MacNab, R.M., Koshland D.E., Common mechanism for repellents and attractants in bacterial chemotaxis. *Science* **181**, 60-63 (1973).
- [8] Blair, D.F. How bacteria sense and swim. *Annu. Rev. Microbiol.* **49**, 489-522.
- [9] Ehrenberg, C.G. *Die Infusionsthierchen als vollkommene Organismen* (Leopold Voss, Leipzig, 1838).
- [10] Macnab, R.M. & Koshland, D.E. Bacterial motility and chemotaxis: light-induced tumbling response and visualization of individual flagella. *J. Mol. Biol* **84**, 399-406 (1974). Macnab, R.M. Examination of bacterial flagellation by dark-field microscopy *J. Clin. Microbiol.* **4**, 258-265 (1976).
- [11] Berg, H.C. Bacteria swim by rotating their flagellar filaments. *Nature* **245**, 380-382 (1973).
- [12] MacNab, R.M. & Ornston, M.K. Normal-to-curly flagellar transitions and their role in bacterial tumbling: stabilization of an alternative quaternary structure by mechanical force. *J. Mol. Biol.* **112**, 1-30 (1977).
- [13] Macnab, R.M. Bacterial flagella rotating in bundles: a study in helical geometry. *Proc. Natl. Acad. Sci. USA* **74**, 221-225 (1977).
- [14] Powers, T.R. to be published.
- [15] Coombs, D. Notes on bundling of flagella, unpublished.

- [16] Turner, L., Ryu, W.S. & Berg, H.C. Real-time imaging of fluorescent flagellar filaments. *J. Bacteriol.* **182**, 2793-2801 (2000).
- [17] Asakura, S., Eguchi, G. & Iino, T. Reconstruction of bacterial flagella *in vitro* *J. Mol. Biol.* **10**, 42-56 (1964).
- [18] Calladine, C.R. Construction of bacterial flagella. *Nature* **225**, 121-124 (1978).
Calladine, C.R. Change of waveform in bacterial flagella: the role of mechanics at the molecular level. *J. Mol. Biol.* **118**, 457-479 (1978). Calladine, C.R. Design requirements for the construction of bacterial flagella. *J. Theor. Biol.* **57**, 469-489 (1976).
- [19] Samatey et al. Structure of the bacterial flagella protofilament and implications for a switch for supercoiling. *Nature* **410**, 331-337 (2001).
- [20] Josephson, Possible new effects in superconducting tunnelling, *Phys. Lett.* **1**, 251-253 (1962).
- [21] Kessler, J.O., personal communication.
- [22] Purcell, E.M. Life at low Reynolds-number *Am. J. Phys.* **45**, 3-11 (1977). Purcell, E.M. The efficiency of propulsion by a rotating flagellum *Proc. Natl. Acad. Sci. USA* **94**, 11307-1311 (1997)
- [23] Goldstein, R.E., Goriely, A., Huber, G. & Wolgemuth, C. Bistable Helices. *Phys Rev. Lett.* **84**, 1631-1634 (2000).
- [24] For general discussions of the motions of thin elastic objects in fluid, with particular application to the case of rotating and bending filaments, the following are valuable: Ref. [33], [38], Powers, T.R. Notes on natural curvature and torsional stress in rotating elastica. (Preprint, 1999). Goldstein, R.E., Powers, T.R. & Wiggins, C.H. Viscous nonlinear dynamics of twist and writhe. *Phys. Rev. Lett* **80**, 5232-5235 (1998).
- [25] Elasticity in the context of low Reynolds number swimming was first studied in Machin, K.E. Wave propagation along flagella. *J. Exp. Biol.* **35**, 796-806 (1958) and Machin, K.E. The control and synchronization of flagellar movement. *Proc. R. Soc. Lond. B* **62**, 88-104 (1962). The swimming effectiveness of a long thin sinusoidal tail was analysed in Taylor, G.I. Analysis of the swimming of microscopic organisms. *Proc. R. Soc. Lond. A.* **209**, 447-461 (1951) and Taylor, G.I. The action of waving cylindrical tails in propelling microscopic organisms. *Proc. R. Soc. Lond. A* **217**, 225-239 (1952). The fluid dynamics of a given swimming shape at low Reynolds number are described in Lighthill, J. *Mathematical biofluidynamics* (SIAM, Philadelphia, 1975). Numerical studies linking elasticity to

- swimming effectiveness are found in a series of papers by Peskin and Fauci [27], [36].
- [26] A review of microcirculatory blood flow is given in T.W. Secomb, *Mechanics of blood flow in the microcirculation*, in *Biological fluid dynamics*, ed. Ellington, C.P. & Pedley T.J. (Company of Biologists, Cambridge, 1995).
- [27] Roma, A.M., Peskin, C.S., Berger, M.J. A three-dimensional computer model of the human heart for studying cardiac fluid dynamics *Comput. Graphics-US* **34**, 56-60 (2000).
- [28] Love, E.M. *A treatise on the mathematical theory of elasticity*. (Dover, New York, 1944).
- [29] Landau, L.D. & Lifshitz, E.M. *Theory of elasticity*, 3rd edition. (Pergamon Press, Oxford, 1986).
- [30] Wardle, K.L. *Differential Geometry*. (Routledge and Kegan Paul, London, 1965).
- [31] In the context of DNA, see Marko, J. & Siggia, E. Bending and twisting elasticity of DNA. *Macromolecules* **27**, 981-988 (1994) and Marko, J. & Siggia, E. Bending and twisting elasticity of DNA. *Macromolecules* **29**, 4820 (1996). For a more general discussion of elasticity of complex molecules, Helfrich, W. Elastic theory of helical fibers. *Langmuir* **7**, 567-568 (1991) and Helfrich, W. Helical bilayer structures due to spontaneous torsion of the edges *J. Chem. Phys* **85**, 1085 - 1087 (1986) are of interest.
- [32] Batchelor, G. *Hydrodynamics* (Cambridge University Press, 1967).
- [33] Wiggins, C.H., Riveline, D., Ott. A. & Goldstein, R.E. Trapping and wiggling: elastohydrodynamics of driven microfilaments. *Biophys. J.* **74**, 1043-1060 (1998) and Wiggins, C.H. & Goldstein, R.E. Flexive and propulsive dynamics of elastica at low Reynolds number. *Phys. Rev. Lett.* **80**, 3879-3882 (1998).
- [34] Rowlinson, J.S. & Widom, B. *Molecular theory of capillarity* (Clarendon Press, Oxford, 1982).
- [35] Kirchhoff, *Über das Gleichgewicht und die Bewegung eines unendlich dunnen elastischen Stabes*, *J. F. Math (Crelle)*, Bd. 56 (1859) is the reference, although I confess I haven't read the original. The details are very thoroughly reviewed in Love [28].
- [36] Fauci, L.J. A computational model of aquatic animal locomotion. *J. Comp. Phys.* **77**, 85-108 (1988).

- [37] Keller, J.B. & Rubinow, S.I. Slender-body theory for slow viscous flow. *J. Fluid Mech.* **75**, 705-714 (1976).
- [38] Wolgemuth, C.W., Powers, T.R. & Goldstein, R.E. Twirling, whirling and flailing: viscous instabilities of rotating elastica. *Phys. Rev. Lett.* **84**, 1623-1626 (2000).
- [39] Holwill, M.E.J. & Burge, R.E. A hydrodynamic study of the motility of flagellated bacteria. *Arch. Biochem. Biophys.* **101**, 249-260 (1963).
- [40] Block, S.M., Blair, D.F. & Berg, H.C. Compliance of bacterial flagella measured with optical tweezers. *Nature* **388**, 514-518 (1989).
- [41] for a nice review of optical trapping applied to biological systems, see Svoboda, K. & Block, S.M. Biological applications of optical forces. *Annu. Rev. Biophys. Biomol. Struct.* **23**, 247-285 (1994).
- [42] Blair, D.F., Block, S.M. & Berg, H.C. Compliance of bacterial polyhooks measured with optical tweezers. *Cytometry* **12**, 492-496 (1991).
- [43] Hoshikawa, H. Elastic properties of bacterial flagellar filaments I. Free rotation case. *Biophysical Chemistry* **17**, 105-109 (1983). Hoshikawa, H. & Kamiya, R. Elastic properties of flagellar filaments II. Determination of the modulus of rigidity. *Biophysical Chemistry* **22**, 159-166 (1985).
- [44] Wolgemuth, C.W., personal communication.
- [45] Fujime, S., Maruyama, M. & Asakura, S. Flexural rigidity of bacterial flagella studied by quasielastic scattering of laser light. *J. Mol. Biol.* **68**, 347-359 (1972).
- [46] see for example, Keener, J.P. *Principles of applied mathematics* (Addison-Wesley, Reading, 1995) or Tabor, M. *Principles and methods of applied mathematics* (Course notes, to be published).
- [47] for a description of how to do this using a symbolic manipulation software package, see for instance Wolfram, S. *The Mathematica book* (Cambridge University Press, 1999).
- [48] Press, W.H., Flannery, B.P., Teukolsky, S.A. & Vetterling, W.T. *Numerical recipes in C*. (Cambridge University Press, Cambridge, 1989).
- [49] Crank, J. & Nicolson, P. A practical method for numerical integration of solutions of the partial differential equations of heat-conduction type. *Proc. Cambridge Phil. Soc.* **43**, 50-67 (1947).

- [50] Burden, R.L. & Faires, J.D. *Numerical Analysis*, 5th edition. (PWS, Boston, 1993).
- [51] For discussions of the analysis of elementary finite difference schemes see Strikwerda, J.C. *Finite difference schemes and partial differential equations*. (Chapman and Hall, New York, 1989), or Smith, G.D. *Numerical solution of partial differential equations : finite difference methods* (Clarendon, Oxford, 1985).
- [52] for the hyperbolic case, see Kreiss, H. *Numerical methods for solving time-dependent problems for partial differential equations* (Universite de Montreal, 1978).
- [53] Fahrner, K.A., Block, S.M., Krishnaswamy, S., Parkinson, J.S. & Berg, H.C. A mutant hook-associated protein (HAP 3) facilitates torsionally induced transformations of the flagellar filament of Escherichia Coli. *J Mol. Biol.* **238**, 173-186 (1994).
- [54] Strick, T.R., Allemand, J.-F., Bensimon, D., Bensimon, A. & Croquette, V. The elasticity of a single supercoiled DNA molecule. *Science* **271**, 1835-1837 (1996).
- [55] Blake, J.R. & Chwang, A.T. Fundamental singularities of viscous flow. *J. Eng. Math* **8**, 23-29 (1974).
- [56] Chwang, A.T. & Wu, T.Y. Hydromechanics of low-Reynolds-number flow. Part 1. Rotation of axisymmetric prolate bodies. *J. Fluid Mech.* **63**, 607-622 (1974).